HHS Public Access
Author manuscript
J Am Chem Soc. Author manuscript; available in PMC 2021 August 12.

Published in final edited form as:
J Am Chem Soc. 2020 August 12; 142(32): 13917–13933. doi:10.1021/jacs.0c06243.

Reaction Mechanism, Origins of Enantioselectivity, and Reactivity Trends in Asymmetric Allylic Alkylation: A Comprehensive Quantum Mechanics Investigation of a C(sp^3)–C(sp^3) Cross-Coupling

Alexander Q. Cusumano,
The Warren and Katharine Schlinger Laboratory for Chemistry and Chemical Engineering, Division of Chemistry and Chemical Engineering, California Institute of Technology, Pasadena, California 91125, United States

Brian M. Stoltz,
The Warren and Katharine Schlinger Laboratory for Chemistry and Chemical Engineering, Division of Chemistry and Chemical Engineering, California Institute of Technology, Pasadena, California 91125, United States

William A. Goddard III
Materials and Process Simulation Center, Beckman Institute, California Institute of Technology, Pasadena, California 91125, United States

Abstract

We utilize quantum mechanics to evaluate a variety of plausible mechanistic pathways for the entirety of the catalytic cycle for asymmetric decarboxylative allylic alkylation of allyl *β*-ketoesters. We present a mechanistic picture that unites all current experimental observations, including enantioinduction, reaction rate, catalyst resting state, enolate crossover experiments, water tolerance, and the effects of solvation on inner- and outer-sphere mechanisms. Experiments designed to evaluate the fidelity and predictive power of the computational models reveal the methods employed herein to be highly effective in elucidating the reactivity of the catalytic system. On the basis of these findings, we highlight a computational framework from which chemically accurate results are obtained and address the current limitations of the decarboxylative asymmetric allylic alkylation reaction.

Graphical Abstract

Corresponding Authors Brian M. Stoltz –, stoltz@caltech.edu; **William A. Goddard, III –**, wag@caltech.edu.

Supporting Information
The Supporting Information is available free of charge at https://pubs.acs.org/doi/10.1021/jacs.0c06243.
Computational details and Cartesian coordinates (PDF)
Quantum mechanical energies (XLSX)

The authors declare no competing financial interest.

Author Manuscript Author Manuscript Author Manuscript Author Manuscript

Author Manuscript Author Manuscript Author Manuscript Author Manuscript

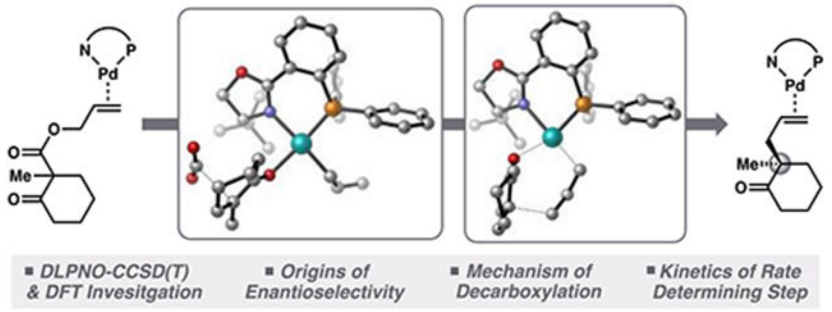

INTRODUCTION

The construction of chiral all-carbon quaternary centers remains a forefront challenge in synthetic chemistry.[1] Over the years, our group has pursued the development of the decarboxylative asymmetric allylic alkylation reaction as a practical entry into these highly sought-after structural motifs. This approach has proved fruitful in asymmetric synthesis,[2] particularly in the early stage preparation of chiral building blocks. However, our efforts to further extend the scope of these transformations have highlighted limitations of the current catalytic systems.[3] We recognize that a comprehensive mechanistic understanding is crucial in our ability to address these shortcomings and to realize general improvements.

Owing to the intricate interplay of several plausible inner- and outer-sphere processes, the unification of a comprehensive, stereochemically complete mechanistic hypothesis has remained elusive for the Pd(PHOX) system. In order to explore the mechanistic subtleties of the Pd(PHOX) system, our group carried out experimental studies geared toward evaluating the prevalence of inner- and outer-sphere pathways. Namely, crossover experiments involving deuterium labeling of both the allyl and enolate fragments ofthe allyl enol carbonate class of masked enolate synthons were explored.[3] The distribution of cross products in these experiments was attributed to either an outer-sphere mechanism, in which C—C bond formation occurs through external nucleophilic attack by a free solvated enolate on an electrophilic π-allyl palladium species, or to an inner-sphere mechanism in which a Pd-bound enolate undergoes C—C bond formation via reductive elimination.[4] Furthermore, the same system demonstrated remarkable tolerance to exogenous water, with reaction yields and enantioselectivity being largely unaffected.[4] These results suggest that the presence of an unbound enolate with a conjugate acid pK_a significantly higher than that of water is unlikely. Given the tolerance to water, an inner-sphere mechanism for C—C bond formation is generally invoked for the Pd(PHOX) system.

In contrast, mechanistic studies with the bis-phosphine (R,R)-ANDEN-phenyl Trost ligand on similar allyl enol carbonate substrates by Trost and co-workers suggest alkylation occurs via an outer-sphere mechanism.[6] As anticipated with an ionic outer-sphere mechanism, highly charge-stabilized “soft” enolates perform well in these systems.[7] However, in contrast to the Trost methods, the PHOX catalytic manifold performs poorly and often provides low levels of enantioselectivity with stabilized enolate nucleophiles,[3,8] yet several PHOX systems excel with more basic “hard” enolates, as well as substrates that contain heteroatoms.[9]

Author Manuscript

Author Manuscript

Author Manuscript

Author Manuscript

Previous quantum mechanics (QM) investigations geared toward evaluating the possibility of an inner-sphere mechanism suggested this hypothesis to be plausible for a related PHOX system.[10] While these investigations provided evidence for an initial mechanistic hypothesis, significant questions pertaining to the practical development of the catalytic system persist. For example, the mechanism by which decarboxylation (the rate limiting process) occurs in the allyl β-ketoester system remains unexplored. A thorough understanding of this process will support our efforts to develop systems with reduced catalyst loading and decreased reaction temperature—key considerations in the scalability of a catalytic transformation. Further convoluted by the complex interplay of several mechanistic pathways, the origin of enantioinduction has yet to be determined. Elucidation of the mechanism by which stereoselectivity is achieved will be central to a systematic approach to ligand design. Lastly, we aim to evaluate the current experimental findings, including water tolerance and crossover experiments, in the context of a thorough mechanistic picture.

Aided by recent experimental advances, including kinetic studies and characterization of intermediate complexes,[4] we turn our attention to the synthetically valuable allyl β-ketoester class of substrates and the (*R*)-*t*-BuPHOX ligand as the basis for a comprehensive computational study (Figure 1a).[3] To provide useful insight into factors underlying enantiomeric selectivity, very high quantum mechanical accuracy is required. Given this, we use this study as an opportunity to compare the efficacy of various modern computational methods (density functional theory and localized coupled-cluster theory) in the context of asymmetric Pd^0/Pd^{II} catalysis.

A detailed QM investigation into each step of the reaction mechanism, oxidative addition, decarboxylation, and C—C bond formation, reveals a mechanistic picture that unites all current experimental observations, including enantioinduction, reaction rate, catalyst resting state, enolate crossover, water tolerance, and solvent effects on the interplay between inner- and outer-sphere pathways in the PHOX system. Experiments are carried out to explore the mechanistic hypotheses derived from the ab initio calculations. Lastly, we address the shortcomings of the present state-of-the-art catalyst systems and offer theory-based insight into future development.

COMPUTATIONAL METHODS

Density functional theory (DFT) geometry optimizations, energy, vibrational frequency, and coupled-cluster calculations were performed using ORCA version 4.1.2.[11] Geometry optimizations were carried out with the BP86 generalized gradient approximation (GGA) functional[12] with Becke-Johnson damped D3 dispersion corrections (herein referred to as D3).[13] A mixed basis set was implemented, in which palladium is described by the small core LANL2TZ(f) basis set with the Hay–Wadt effective core potential (ECP),[14] while the 6-31G(d) basis set was used on all other atoms. Key structures were optimized at various levels of theory and compared to crystallographic data to ensure that consistent results are obtained across multiple methodologies (see SI for details).

Triple-ζ quality single point calculations were carried out on all stationary points with a variety of density functionals, including BP86-D3,[12] B3LYP-D3,[15] PBE0-D3,[16] M06,[17] and

Author Manuscript

Author Manuscript

Author Manuscript

Author Manuscript

DSD-BLYP-D3[18] (see SI for comprehensive list) with the def2-TZVP basis set[19] on all atoms (including the small core def2-ECP[20] on palladium). Corrections for solvation (THF or otherwise as specified) were carried out for single point calculations with the implicit Conductor-like Polarizable Continuum Model (CPCM).[21] Unless otherwise noted, all energies reported are G_{298} values from single point calculations at the M06/def2-TZVP–CPCM(THF) level of theory on BP86-D3/LANL2TZ(f)–6-31G(d) optimized geometries with thermodynamic corrections applied from frequency calculations obtained at the optimization level of theory. The Quasi-RRHO method is applied to correct for the breakdown of the harmonic oscillator approximation for low frequency vibrations.[22] All stationary points are characterized by the appropriate number of imaginary vibrational modes (zero for optimized geometries and one for transition states). Intrinsic reaction coordinate (IRC) analyses were carried out to ensure all transition states connect the appropriate starting materials and products. Molecular illustrations were made from CLYview.[23]

Additional single point calculations were performed on all optimized structures with the domain based local pair natural orbital coupled-cluster (DLPNO-CCSD(T), “NormalPNO” settings unless otherwise noted) method as described by Neese and co-workers and as implemented in ORCA (further details included in the SI section).[24] The cc-pVTZ basis set is used on all atoms in the DLPNO-CCSD(T) calculations, with the SK-MCDHF-RSC effective core potential[25] on palladium. Throughout the text, free energies calculated from electronic energies at the DLPNO-CCSD(T)/cc-pVTZ–CPCM(THF) level of theory are provided in brackets next to the DFT (M06–CPCM(THF)) values for comparison.

RESULTS

Our investigation began with the experimental observation of the [(PHOX)Pd(η^1-allyl)(RCO_2)] complex (**3**) as the resting state of the catalyst (Figure 2). The structure of this unusual η^1-allyl complex was previously confirmed by X-ray crystallography while the solution phase behavior was studied by NMR spectroscopy.[4] Importantly, **3** is competent in the reaction, and affords the ketone product 2 from β-ketoester **1** in similar yield and enantioselectivity to that obtained from the catalytic transformation. Also noteworthy is the thermal instability of **3**, which readily effervesces gaseous carbon dioxide at ambient temperatures to afford the ketone product. Kinetic studies revealed first order rate dependence of this process in **3**,[5] with an overall rate constant measured to be 1.58×10^{-4} s^{-1} (at 24 °C in THF-d_8).[4] Given that loss of CO_2 is the rate-limiting step, the experimental $\Delta G^{\ddagger}$ of decarboxylation is calculated to be 22.6 kcal/mol.

Oxidative Addition.

To better understand the role of the catalyst resting state (**3**) in the overall mechanistic picture, we first sought to examine the mechanism of oxidative addition of allyl β-ketoester **1** to the Pd^0(PHOX) precatalyst. Oxidative addition of allyl acetate to palladium(0) complexes is generally represented as directly generating the [$L_nPd(\eta^3$-allyl)](OAc) ion pair in situ in a reversible fashion.[26] Interestingly, we observed that the square planar η^1-allyl form of the catalyst is the exclusive resting state (**3**) (Figure 2). This prompted us to question

Author Manuscript

Author Manuscript

Author Manuscript

Author Manuscript

whether oxidative addition proceeds through a unique mechanism in which **3** is yielded directly or if an analogous [(PHOX)Pd(η^3-allyl)]$^+$(RCO$_2^-$) ion pair (**4**) is first formed followed by rapid equilibration to **3** (Figure 2). An understanding of the mechanics of oxidative addition is critical in the validation and interpretation of experimental findings because retention/inversion of the stereocenter at the leaving group site is often utilized as a mechanistic probe to infer the presence of inner- or outer-sphere pathways.[6,27]

As noted previously, racemic starting material **1** is employed in the reaction. Nevertheless, as the chiral center is not directly involved but rather appended to the site of oxidative addition through freely rotatable bonds, we expect comparable energies of the diastereomeric transition states arising from both enantiomers of the starting material **1**. As such, our initial explorations considered the (*R*) enantiomer of **1**. For completeness, the relevant oxidative addition pathways studied for (*R*)-**1** are also evaluated for (*S*)-**1**. A similar consideration is employed with regard to the orientation of the allyl fragment in the η^3-bound form. Here, the prefix *endo* describes the η^3-(allyl) conformer in which the apical carbon (i.e., C2) of the allyl group is *cis* to the *t*-Bu group of the PHOX ligand, and *exo* the *trans* isomer. Experimentally, the *endo* and *exo* isomers were found to be nearly identical in energy. Thus, both *endo* and *exo* geometries will be considered where relevant.

Starting from olefin-bound Pd^0(PHOX) complex **5**, a variety of transition states that achieve C—O bond cleavage were considered (Figure 3). Three- (**TS1**) and seven-membered (**TS2**) cyclic transition states[28-30] afford barrier heights greater than that of the experimentally known rate-determining step ($\Delta G^\ddagger$ = 22.6 kcal/mol).[4] Oxidative addition via a *syn* conjugate displacement-type mechanism (**TS3**) offers a lower energy alternative, yet with a $\Delta G^\ddagger$ of 21.6 [22.1] kcal/mol, it remains unlikely.

Analogous to **TS3**, an *anti* displacement-type mechanism (**TS4**) via electrophilic addition to Pd^0 was investigated and found to possess substantially lower barrier heights to that of the other pathways considered (Figure 4). Unlike **TS3**, in which C—O bond breaking occurs through the filling of σ*(C–O) by the olefin-based π*(C–C) orbital, **TS4** achieves the same overall result with direct overlap between σ*(C–O) and the palladium $d_{x^2-y^2}$ -based HOMO.

Isomeric transition states are possible in which the displacement event occurs *trans* to either the nitrogen or phosphorus of the PHOX ligand to afford either the *endo* or *exo* isomer of **4**. The abbreviations *t*-N and *t*-P refer to C—O bond breaking occurring *trans* to N and *trans* to P, respectively. Likewise, the prefix *endo/exo* describes the predisposition of the transition state to yield the *endo/exo* π-allyl **4**. This nomenclature is extended to describe the orientation of the precursor olefin-bound complexes, **5**. Here, we assume free equilibration between the isomers of **5**. Therefore, we consider the apparent barrier height to be that of the lowest energy transition state from the lowest energy isomer of **5**, **(exo/*t*-N)-5**.

From the corresponding olefin-bound palladium precursors **5**, we found barrier heights of 13.8 [13.3] and 11.5 [10.3] for **(exo/*t-P*)-TS4** and **(endo/*t-P*)-TS4**, respectively. Interestingly, considerably lower energy pathways were obtained for displacements *trans* to nitrogen, with barriers to **(exo/*t-N*)-TS4** and **(endo/*t-N*)-TS4** of 6.4 [4.8] and 7.1 [4.4] kcal/mol. In total, the lowest energy pathway of oxidation addition via direct displacement starts

Author Manuscript Author Manuscript Author Manuscript Author Manuscript

with **(exo/*t*-N)-5** to form the ion pair product **(exo)-4** via **(exo/*t*-*N*)-TS4** with an apparent $\Delta G^{\ddagger}$ of 6.4 [4.8] kcal/mol and ΔG of −1.0 [−5.8] kcal/mol. A similar energetic preference for displacement *trans* to nitrogen is observed across several DFT methods. Additionally, as anticipated by experiment, the energy of **(exo)-4** and **(endo)-4** were found to be nearly identical, with the *exo*-isomer favored by 0.3 [0.4] kcal/mol. Henceforth, reference to **TS4** will specifically refer to the lowest energy isomer, **(exo/*t*-*N*)-TS4**.

In summary, of all the oxidative addition pathways considered, olefin binding, followed by *anti* displacement (TS4) affords the lowest barrier height by a considerable margin. The displacement is stereospecific to inversion of chirality with respect to that of the leaving group, whereas the pathways involving a three-centered transition state (**TS1**), a 7-membered pericyclic transition state (**TS2**), or a *syn* conjugate displacement (**TS3**) would be expected to retain the configuration of the carboxylate leaving group (when substitution is present on the allyl terminus). We emphasize that the consideration of each mechanistic pathway is crucial in order to reliably interpret net inversion/retention of stereochemistry as a general mechanistic probe in the Tsuji–Trost reaction.

Furthermore, the two lowest energy pathways (direct/*anti* and conjugate/*syn* displacement) directly afford the ion pair **4** rather than **3** as the product of oxidative addition. These results suggest that the observed η^1-(allyl) catalyst resting state (**3**) is *not* the direct product of oxidative addition but is rather generated through a subsequent equilibration from ion pair **4**. To realize the magnitude of the difference in energy between η^1-allyl **3** and ion pair **4**, and whether a similar preference for **3** would be found computationally, we compare the calculated free energies of the two complexes. We arrive at the same result, in which [(PHOX)Pd(η^1-allyl)(RCO_2)] (**3**) is favored over the [(PHOX)Pd(η^3-allyl)]$^+$(RCO_2^-) ion pair **4** by 5.4 kcal/mol (Figure 5). Single point calculations with several other density functionals give rise to similar results (ΔG = 4.6 to 9.3 kcal/mol), showing that this outcome is not an artifact of the DFT functional. A difference in free energy of 5.2 kcal/mol favoring **3** is obtained at the DLPNO-CCSD(T) level of theory, in agreement with the DFT values.

Interestingly, this trend appears not to be an extraneous effect of the β-ketocarboxylate leaving group but rather a potential feature of the PHOX ligand framework. Control experiments have been previously reported by our group in which the allyl β-ketoester was replaced with allyl acetate to similar effect.[4] The corresponding [(PHOX)Pd(η^1-allyl)(OAc)] complex (**6**) was isolated and characterized by X-ray crystallography and solution phase NMR spectroscopy.[4] Accordingly, the difference in free energies between **6** and ion pair **7** was calculated to be 6.6 [6.0] kcal/mol, favoring the η^1-allyl form.

Since computational results were in excellent agreement with experiment, we sought to explore these trends for the allyl enol carbonate substrate class,[31] for which a crystal structure of the catalyst resting state has yet to be obtained. As with the β-ketocarboxylates, the analogous [(PHOX)Pd(η^1-allyl)-($ROCO_2$)] (**8**) was similarly predicted to be favored over the [(PHOX)Pd(η^3-allyl)]$^+$($ROCO_2^-$) ion pair (**9**) (Figure 5). Calculations with the M06 density functional predict a 0.6 kcal/ mol preference for the η^1-allyl form, while DLPNO-CCSD(T) theory refines the energy difference to 2.5 kcal/mol, still favoring the η^1-allyl form. Accordingly, ^{31}P NMR studies suggest the catalyst resting state may be an analogous

Author Manuscript

Author Manuscript

Author Manuscript

Author Manuscript

η^1-allyl complex.[4] Taking experimental and theoretical results into account, we anticipate that **the η^1-allyl form similarly dominates the solution phase character of the catalyst resting state.**

It is important to note that complexes **3**, **4**, **8**, and **9**, are constitutional isomers. Since the subsequent reaction yields identical palladium enolate intermediates, we note that the enol carbonate substrate is predicted to undergo a more exergonic reaction than the β-ketocarboxylate isomer by *ca.* 10 kcal/mol. While investigation into the mechanism of decarboxylation of the enol carbonates **8/9** lies outside the scope of this investigation, we postulate the following: *If* the resting state of the catalyst in the enol carbonate system is described by **8/9** (analogous to the carboxylates), and *if* the absolute energy of the barrier to decarboxylation is similar to that of **3**, then a significantly higher reaction rate is anticipated. We therefore wish to highlight the design of the enolate synthon as one avenue by which future improvements may be achieved.

Decarboxylation.

We then sought to explore the mechanism through which decarboxylation occurs. Loss of CO_2 was experimentally determined to be the rate-limiting step of catalyst turnover.[4] Thus, theory-guided optimization of the decarboxylation step may offer the practical benefit of increased reaction rate. In turn, this brings secondary advantages of potentially lower catalyst loading and reduced reaction temperature. Furthermore, certain classes of allyl β-carbonyl ester substrates, such as lactones and other particularly electron rich enolates, fail to decarboxylate or require higher reaction temperatures.[32] In order to address these limitations and capitalize on opportunities for future development, a detailed mechanistic understanding of the decarboxylative pathways is required.

As noted previously, the minimum energy pathways in the first step of the mechanism through oxidative addition directly afford ion pair **4**, rather than the catalyst resting state **3**. To explore the interconnectivity between these intermediates, as well as potential decarboxylative pathways, we constructed the free energy network depicted in Scheme 1.

Deriving inspiration from the canonical 6-membered ring transition states in the decarboxylation of β-ketocarboxylic acids, we considered analogous cases for palladium (Figure 6). Two isomeric square pyramidal transition states may be envisioned: one in which the carboxylate group is apically bound to palladium (**TS5**), and another with an equatorially bound carboxylate (**TS6**). Both transition states require the square pyramidal precursors **10** and **11**, respectively (Scheme 1). Sufficiently low energy pathways connecting resting state **3** to the necessary decarboxylation precursor **10** are found (Scheme 1).

Decarboxylation is observed only through transition states in which the carboxylate group is poised axially on the 6-membered ring, whether it be in a boat ((**boat**)-**TS5**) or chair ((**chair**)-**TS5**). This may result from orbital overlap requirements, since the $C–CO_2^-$ σ orbital experiences enhanced overlap with the π^* of the ketone when occupying an axial position. While the chair conformers dominate the equilibrium geometries of **10**, both M06 and DLPNO-CCSD(T) methods predict decarboxylation through **(boat)-TS5** to be lower in energy than **(chair)-TS5** by 1.8 and 2.8 kcal/mol, respectively, with corresponding apparent

Author Manuscript Author Manuscript Author Manuscript Author Manuscript

$\Delta G^{\ddagger}$ values of 22.0 and 26.8 kcal/mol (from resting state **3**). We will henceforth refer to this sequence as **decarboxylative pathway 1**.

While the barrier to decarboxylation via **(boat)-TS5** is quite low with respect to **10** (5.9–9.9 kcal/mol), decarboxylation directly from **11** is not observed. This result is not unexpected, since weak axial binding is generally observed in square planar d^8 complexes (in the absence of π back bonding) by virtue of the filled, axially oriented metal-based d_{z^2} orbital, here of slight Pd—O σ^* character. With consideration of the role of the Pd^{II} center as a Lewis acid in promoting the decarboxylation, the weak axial binding of the ketone carbonyl in **11** to the metal center results in a complex that is poorly predisposed to decarboxylation. Furthermore, the LUMO of the square-planar/square-pyramidal d^8 complexes are largely of metal-based $d_{x^2-y^2}$ character. As such, compared to **11**, the equatorially bound carbonyl of **10** exhibits greater overlap with the Pd-based LUMO, allowing for more effective charge transfer to the electropositive metal center. This, combined with the greater positive partial charge of the palladium center in **10**, due to the weakly bound axial carboxylate counterion, results in facile decarboxylation.

Analogous to the highly charge-separated cyclic form of **10**, we were intrigued to find an acyclic variant, **12**, as a stable intermediate on the potential energy surface. Given the complete potential energy surface (PES), we presume **12** equilibrates with resting state **3** through the lower energy **TS11-11-TS12-4-TS13** pathway (Scheme 1). Here, the highest barrier is that of **TS13** at 14.0 [16.3] kcal/mol, with **12** at 12.7 [15.9] kcal/mol higher in energy than **3**.

As with **10**, decarboxylation from **12** may then occur with the carboxylate oriented axially in either a chair or boat conformer, with the chair being lowest in energy (**TS14**). From **12**, a barrier height of 4.4 [6.1] kcal/mol through **TS14** is found. With respect to resting state **3**, the overall barrier to decarboxylation through this pathway is 17.1 [22.0] kcal/mol. As with **TS5**, decarboxylation through this route directly affords the η^1-(allyl) O-bound palladium enolate **(*Si*)-13** (a stable rotamer of **(*Re*)-13**). We will henceforth denote this sequence as **decarboxylative pathway 2**.

We next envisioned the possibility for decarboxylation to occur directly from the $[(\eta^3\text{-allyl})\text{Pd(PHOX)}]^+(\text{RCO}_2^-)$ ion pair, **4**. We will term this sequence **decarboxylative pathway 3**. In pathway 3, the overall barrier height through decarboxylation was found to be 17.5 [23.2] kcal/mol via the lowest energy conformer of **TS15**. Dissimilar to pathways 1 and 2, pathway 3 does not lead directly to **(*Re/Si*)-13** but rather the η^3-allyl isomer **14**. The relevance of this detail becomes apparent below in the free energy networks through which C—C bond forming occurs (Scheme 2).

Loss of CO_2 is the overall rate-determining step for pathways 1, 2, and 3.—Of the three, we found pathway 2 to have the lowest barrier at 17.1 [22.0] kcal/mol; however, pathway 3 is comparable in energy, with a barrier height of 17.5 [23.2] kcal/mol, and the difference between these pathways is likely within the accuracy of DFT. Single point calculations with B3LYP-D3, PBE0-D3, and DSD-BLYP-D3 favor **TS14** by 5.0, 2.0, and

Author Manuscript

Author Manuscript

Author Manuscript

Author Manuscript

0.4 kcal/mol, respectively; thus, we suggest an energetic preference for pathway 2. However, both pathways 2 and 3 remain mechanistically relevant under the reaction conditions.

Since the dipole moment of **TS15** (19.7 D) is large compared to those of **TS5** (12.2 D) and **TS14** (13.6 D) (with M06/CPCM(THF)) we investigated the effect of solvation on the relative free energy barriers of the three pathways. Experimentally, high yields and enantioselectivities are observed across a variety of nonpolar aprotic solvents, while yields and enantioselectivities diminish in polar, aprotic solvents.[3]

Our initial efforts to assess solvent dependence were focused on solvent effects from single point calculations using the implicit Conductor-like Polarizable Continuum Model (CPCM) for geometries optimized in the gas phase. As stated above, we found net barrier heights of 17.1, 17.5, and 22.0 kcal/mol in THF ($\varepsilon = 7.3$) for decarboxylation pathways 2, 3, and 1, respectively. Control computation experiments were carried out in which optimizations of select intermediates were additionally carried out in THF (see SI), yielding similar results.

In addition to THF ($\varepsilon = 7.3$), we compared the barrier heights of the three decarboxylative pathways in the less polar solvents toluene ($\varepsilon = 2.4$) and diethyl ether ($\varepsilon = 4.3$), along with the more polar DMF ($\varepsilon = 38.3$). A clear trend arises in which a continuum with a reduced charge permittivity ($\varepsilon < 8$) favors pathway 2 (**TS14**), while pathway 3 (**TS15**) is preferred in solvents with higher dielectric constants ($\varepsilon > 8$) (Figure 7).

Specifically, **TS14** is 4.2 kcal/mol lower in energy than **TS15** in toluene, compared to $\Delta\Delta G^{\ddagger}$ values of 1.8 and 0.4 kcal/mol (favoring **TS14**) in Et_2O and THF, respectively. In DMF, pathway 3 is predicted to be most favorable, with **TS15** being 1.3 kcal/mol lower in energy than **TS14**. Furthermore, we found these trends to be a result of the simultaneous lowering of the barrier of **TS14** and raising that of **TS15** with decreasing solvent polarity. For example, $\Delta G^{\ddagger}$ of decarboxylation through **TS14** with M06/def2-TZVP–CPCM(toluene) was found to be 15.4 kcal/mol, compared to 17.1 kcal/mol in THF. Meanwhile, the barrier height to **TS15** is 19.6 kcal/mol in toluene, compared to 17.5 kcal/mol in THF. In conclusion, less polar solvents afford greater selectivity for pathway 2 while lowering the overall barrier height to decarboxylation through this pathway.

Since the polarizable continuum implicit solvation model considers electrostatics as the sole component of solute–solvent interaction, it may be inadequate to *quantitatively* capture all effects in the experimental solvent variations. We expect the general trends to remain qualitatively consistent with these findings and, thus, valuable for considerations in future reaction development.

As previously mentioned, decarboxylation was found experimentally to be the rate-determining step of catalytic turnover. NMR experiments determined the rate constant of decarboxylation of isolated **3** in THF-d_8 to be 1.58×10^{-4} s^{-1} at 24 °C, corresponding to $\Delta G^{\ddagger} = 22.6$ kcal/mol, which is consistent with the observed reaction time of 8–12 h. Indeed, this experimental observation affords an opportunity to compare the computational methods utilized in this study. Interestingly, all density functionals employed predict lower barriers than that of experiment. The most accurate values are obtained with the global hybrid PBE0-

Author Manuscript Author Manuscript Author Manuscript Author Manuscript

D3 and the spin-component-scaled double-hybrid DSD-BLYP-D3, with calculated barriers of 20.2 and 18.6 kcal/mol, respectively. The popular B3LYP-D3 density functional affords the least accurate $\Delta G^{\ddagger}$ of 16.5 kcal/mol. With a barrier of 17.1 kcal/mol, M06 also overestimates the rate of decarboxylation. Calculations with DLPNO-CCSD(T) provide a barrier height of 22.0 kcal/mol ($k_{calc} = 4.65 \times 10^{-4}\ \mathrm{s}^{-1}$) in good agreement with experiment and are the most accurate of the methods tested.

As racemic allyl *β*-ketoester **1** is employed in the stereoablative transformation, we carried out an analogous investigation for the (*S*) enantiomer of **1**. A qualitatively similar situation is encountered. Details are included in the Supporting Information section.

Previous mechanistic studies found both the reaction yield and product enantioenrichment to be tolerant of super-stoichiometric equivalencies of water.[4] This result formed the basis of evidence for an inner-sphere mechanism. Additionally, crossover experiments with deuterium labeling of both the allyl fragment and enolate were performed. Since nearly equal quantities of the crossed products were observed, the involvement of an outer-sphere mechanism in which a solvated free enolate is indifferent to attacking either the labeled or unlabeled η^3-allyl complexes may be considered but is inconsistent with the water-stability of the system. As previously noted,[4] these results may also be accommodated within the inner-sphere mechanistic hypothesis as well. This may be the case when the carboxylate/carbonate intermediates are sufficiently stable to undergo exchange prior to decarboxylation.

For the *β*-ketocarboxylate intermediate, this mechanism appears to take place. With a comparison of the difference in free energy between ion pair **4** and solvent separated ions **15** and **16**, it is reasonable that free exchange between the carboxylate anion and palladium cation may occur at a rate superseding that of decarboxylation (Scheme 1). Both inner- and outer-sphere mechanisms may thus accommodate the results of the crossover experiments. Therefore, under these conditions, the observation of the enolate/allyl electrophile crossover is irrelevant to differentiation between the two mechanistic pathways.

With regard to water tolerance, we compared the barrier heights to decarboxylation for the conjugate acid of *β*-ketocarboxylate **16** (**16-H**) via the canonical 6-membered cyclic transition state to those of the palladium catalyzed pathways mentioned above. With $\Delta G^{\ddagger}$ = 20.3 [26.1] kcal/mol for **TS16**, the lowest apparent barriers to decarboxylation remain those involving the palladium catalyst (pathways 2 and 3). Furthermore, the lower pK_a of **16-H** compared to water (ca. 10 units) affords a low effective concentration **16-H** and, thus, a substantially slower reaction than that indicated from the relative $\Delta G^{\ddagger}$ from **16-H** is expected. This offers an explanation as to why, in the Pd(PHOX) catalyzed systems, the decarboxylated but nonalkylated starting material is not observed. Hence, the experimentally observed water tolerance is well explained for this system.

C—C Bond Formation.

Given the postdecarboxylation palladium enolate intermediates **14**, **(*Re*)-13**, and **(*Si*)-13**, we then sought to explore possible mechanisms for C(sp^3)–C(sp^3) bond formation. We further exploit this opportunity to revise and expand upon previous investigations in this area.[10]

Author Manuscript Author Manuscript Author Manuscript Author Manuscript

First, inner-sphere mechanisms are considered. We envisioned four unique classes of transition states through which reductive elimination may occur: (i) a 3-membered ring transition state from a C-bound Pd enolate (**TS17**), (ii) a 5-membered cyclic transition state from a C-bound Pd enolate in which the carbon atom of the palladium enolate migrates to the γ-carbon of the allyl fragment (**TS18**), (iii) a different 5-membered ring transition state from an O-bound Pd enolate in which the carbon atom of the enolate bonds with the α-carbon of the allyl fragment (**TS19**), and (iv) a 7-membered cyclic transition state (**TS20**)[33] (Figure 8). Previous investigation suggests that the isomerization between oxygen and carbon-bound palladium enolates is facile.[10] Thus, we initially focused on evaluating the $C(sp^3)$–$C(sp^3)$ bond forming event.

Consistent with previous observations,[10] three-centered transition state **TS17** was calculated to be intractably high in energy, with an apparent barrier of 33.7 [46.4] kcal/mol. To determine whether a lower energy transition state could be found by expanding the ring size, we considered the vinylogous case of the 5-centered transition state (**TS18**). However, the planarity of the allyl fragment in the transition state mandates a still highly strained 5-membered ring. Despite our best efforts, a transition state fitting this connectivity was never found on the PES, and any transformation similar would likely be intractably high in energy. Next, we turn our attention to an alternative 5-membered cyclic transition state, **TS19**. Beginning from the O-bound palladium enolate **13**, the barrier to **TS19** is found to be 32.6 [46.3] kcal/mol and, thus, is likely not responsible for C—C bond formation.

Lastly, we considered the fully expanded 7-membered cyclic transition state, **TS20**. Here, the 7-membered ring may adopt either a boat or chair conformer for both *Re* and *Si* faces of the enolate. Additionally, the 6-membered ring of the cyclohexanone enolate fragment may adopt two unique half chair conformers, giving rise to eight total transition states to be considered (Figure 9). Here, bond formations from the *Re* and *Si* faces afford the *S* and *R* enantiomers of product, respectively. The prefixes *chair/boat* refer to the conformation of the 7-membered ring, and *axial/equatorial* denote the half chair geometry of the cyclic enolate.

Transition states that feature *equatorial* attack of the allyl fragment by the enolate half chair are all higher in energy than their *axial* counterparts by 0.4 to 1.5 kcal/mol. Henceforth, in our discussion, the *axial/equatorial* suffix will be omitted with all references being to the favorable *axial* transition states. In comparison with the previously mentioned inner-sphere transition states, all eight of the 7-membered cyclic transition states (**TS20**) offer substantially lower barriers to C—C bond formation, with $\Delta G^{\ddagger}$ ranging from 10.8 [18.5] to 15.1 [24.6] kcal/mol.

Experimentally, the (*R*)- enantiomer of the *t*-BuPHOX ligand yields (*R*)-2-allyl-2-methylcyclohexan-1-one (**(R)-2**) as the major product with 88% ee. At a reaction temperature of 25 °C, this corresponds to an effective energetic difference of 1.6 kcal/mol between the enantiodetermining transition states. Albeit, this assumes a single predominant pathway to the enantioenriched product.

From O-bound Pd enolate **(*Si*/*Re*)-13**, we found the lowest energy difference between *Re/Si* diastereomeric transition states to be **(*Si*/chair)-TS20** and **(*Re*/boat)-TS20**, with barrier

Author Manuscript
Author Manuscript
Author Manuscript
Author Manuscript

heights of 10.8 and 12.1 kcal/mol, respectively ($\Delta\Delta G^{\ddagger}$ = 1.3 [1.9] kcal/mol) (Figure 9). This initial result is in good agreement with the experimentally observed enantioselectivities.

Because the reliable obtaining of relative energies within a subkcal/mol error from QM is challenging, we performed a variety of control calculational experiments. Single point calculations on the BP86-D3/LANL2TZ(f)-6-31G(d) optimized geometries were carried out with a suite of 15 density functionals, encompassing several classes of functionals. Electronic energies obtained at the DLPNO-CCSD(T) level of theory (with both "NormalPNO" and "TightPNO" settings) were employed for benchmarking. The four lower energy *axial* conformations of **TS20** (Figure 10) were also optimized with a subset of density functionals (with and without empirical dispersion corrections (D3)), followed by single point calculations as previously described (see SI for details). All results from the control experiments correctly predict **(*Si*/chair)-TS20** to be the overall lowest energy transition sate, with **(*Re*/boat)-TS20** as the lowest energy pathway for the formation of the minor product **(*S*)-2** (see SI for details). Thus, **we propose C—C bond formation via TS20 to be the enantiodetermining step in the decarboxylative asymmetric allylic alkylation reaction with the Pd(PHOX) catalyst** (Figure 9).

An investigation of a related system by our groups highlighted internal rearrangements of a palladium enolate as a potential mechanism by which product enantioselectivity is determined.[10b] Although outside the scope of that investigation, the authors noted that a subsequent equilibration between (*Si/Re*) enolates may be facile. Thus, a definite conclusion as to the origin of the enantioinduction was not drawn. Accordingly, we found a facile interconversion between **(*Si*)-13** and **(*Re*)-13**, with a rotational barrier several kcal/mol lower in energy than that of C—C bond formation (**TS24**) (Scheme 2). Therefore, the rate of kinetic quenching of intermediates **(*Si*)-13** and **(*Re*)-13** will not be sufficient to preserve any stereochemical induction of previous mechanistic steps.

Upon further examination, it becomes clear that in the case of the favored **(*Si*)-TS20** geometries, adverse interaction between the α-methyl substituent of the enolate fragment and the *t*-Bu group of the PHOX ligand is minimal compared to the analogous clash between the *t*-Bu group and the carbocyclic backbone of the enolate found in **(*Re*)-TS20**. The four atoms ligating palladium, along with the two carbon termini of the newly forming σ(C—C) bond, are nearly coplanar (Figure 11). In the *Re* transition states, the resulting steric clash between the ligand and substrate leads to a distorted chair/boat transition state as well as deviation from square planarity at the palladium center. We performed a control calculation in which the *t*-Bu group of the PHOX ligand was replaced with a hydrogen atom, followed by subsequent transition state optimization. The [des-*t*-Bu] suffix is used to describe these geometries. The **(*Re*/chair)-TS20-[des-*t*-Bu]** structures regain similar planarity and relative energies to that of the **(*Si*/chair)-TS20-[des-*t*-Bu]**, with **(*Re*/chair)-TS20-[des-*t*-Bu]** being 1.4 [0.5] kcal/mol lower in energy than the (*Si*/chair) counterpart. With the *t*-BuPHOX ligand, the relative barrier heights of the diastereomeric chair transition states are 2.1 [2.8] kcal/mol apart in energy, favoring the (*Si*) enolate. These results suggest that the steric interaction from the carbocyclic scaffold and the *t*-Bu group of the PHOX ligand, along with the accompanying distortion from square planarity, is the primary origin of enantioinduction.

Author Manuscript

Author Manuscript

Author Manuscript

Author Manuscript

Although previous work suggests an inner-sphere mechanism to be prevalent, we do not discount the possibility that a competing outer-sphere mechanism is also present. In fact, with the Pd(PHOX) system, stabilized “soft” enolates generally remain competent in the reaction, albeit with substantially reduced enantioselectivities.[3] In the canonical Tsuji–Trost allylic alkylation, differentiation between inner- and outer-sphere pathways is highly reliant on the nature of the nucleophile,[34] with hard nucleophiles proceeding through inner-sphere attack and soft nucleophiles via outer-sphere mechanisms. As such, we hypothesize that the poor enantioselectivities observed with stabilized enolates are likely the result of a less selective outer-sphere mechanism dominating the C—C bond formation step. In an effort to continue the development of this methodology to include previously inaccessible substrate classes, we sought to explore the intricacies of the interplay between outer-sphere and inner-sphere mechanisms.

From O-bound enolates **(*Si*)-13** and **(*Re*)-13**, an associative displacement of the enolate by the olefin of the allyl fragment (**(*Si/Re*)-TS21**) directly affords **14** (as two inconsequential rotamers) (Scheme 2). Its noteworthy that **14** is also the product of decarboxylation through **TS15** (decarboxylative pathway 3) (Scheme 1). As expected, in **14**, bonding between the axial enolate oxygen and Pd is dominated by electrostatic attraction. Intermediate **14** presents a Pd—O bond length of 2.72 Å and Löwden bond order of 0.23, compared to the 2.08 Å Pd–O bond length and bond order of 0.60 as observed in **(*Si*)-13**. As such, disassociated ions **15** and **17** are comparable in free energy to **14**. This was found to be the lowest energy entry into the outer-sphere mechanistic space (Scheme 2).

In considering C—C bond formation through an outer-sphere attack of enolate **17** on the [(η^3-allyl)Pd(PHOX)]$^+$ complex (**15**), we note that attack may occur either *trans* to N (*t*-N) or *trans* to P (*t*-P), from the *Si* or *Re* face of the enolate, in both enolate half chairs, and to either *exo* or *endoallyl* **15**. On the basis of our previous findings, we considered only the enolate half chair which gives rise to the favored axial attack. Here, we found six of the eight hypothesized transition states for this outer-sphere process (**TS22**).

Unlike the inner-sphere transition states **TS20**, which give rise to $\Delta\Delta G^{\ddagger}$ of 1.3 [1.9] kcal/mol between the lowest energy diastereomeric transition states, the outer-sphere transition states afford reduced selectivity. From transition states **(exo/*Si*/*t*-P)-TS22** and **(endo/*Re*/*t*-N)-TS22**, a $\Delta\Delta G^{\ddagger}$ of 0.6 [1.4] kcal/mol was calculated.

In addition to reactivity at the π-allyl carbon termini, nucleophilic attack at the central carbon of the allyl fragment to afford palladacyclobutane species is known.[35] Previous experimental and computational studies find the mode of reactivity to be highly dependent on the σ-donating/π-accepting nature of the ancillary ligand and the basicity of the nucleophile.[35] Palladacyclobutane complexes have been proposed as mechanistic intermediates in palladium-mediated cyclopropanation reactions,[36] as well as isolated and characterized by X-ray crystallography.[37]

With relevance to this work, we considered that **15** and **17** may combine in such a way that the oxygen atom of **17** forms a covalent bond with the β carbon of the allyl fragment to

Author Manuscript Author Manuscript Author Manuscript Author Manuscript

afford metallacyclobutane **18**. Here, the prefix endo/exo describes the relative stereochemistry at the central carbon atom of the allyl fragment of the η^3-allyl precursor **15**.

In this conformation, the C—C π orbitals of the enolate fragment are in potentially good overlap with the Pd—C σ* of the allyl terminus. Thus, we envisioned intermediate **18** may be a competent precursor to the desired C—C bond formation via **(*Si*/Re)-TS23**. IRC analysis reveals that **(*Si*/Re)-TS23** directly connects metallacyclobutane **18** and the complexed ketone product **(*R*/*S*)-19** on the potential energy surface without the intermittency of ion pair **15+17**. Therefore, **TS23** represents a C—C bond forming pathway unique to that of **TS22**. Complex **18** is well poised for reductive elimination to form **19**. The apparent barrier to this process (relative to enolate **(*Si*)-13**) is 16.4 [20.5] and 16.1 [20.8] kcal/mol for **(endo/*Si*/*t*-P)-TS23** and **(endo/*Re*/*t*-P)-TS23**, respectively.

From analysis of the free energy network encompassing palladium enolates **(*Si*)-13**, **(*Re*)-13**, and **14**, with the accompanying C—C bond forming pathways, the following conclusions are drawn:

1. Given facile rotation about the Pd—O and C—O σ bonds in palladium enolates **(*Si*)-13** and **(*Re*)-13**, preservation of stereochemical information through differentiation in energy between prior diastereomeric transition states should largely be erased. We found the rotational barrier from **(*Si*)-13** to **(*Re*)-13** to be 5.1 [6.6] kcal/mol (via **TS24**), whereas the minimum energy barrier to C—C bond formation is 10.8 [18.5] kcal/mol. Therefore, the rate of kinetic quenching of intermediates **(*Si*)-13** and **(*Re*)-13** will not be sufficient to preserve any stereochemical induction from previous mechanistic steps. However, this feature of the PES may be substrate specific and more extrapolated scaffolds may experience rotational barriers similar to or greater than that of C—C bond formation.
2. The mechanism through which decarboxylation of the β-ketoester occurs plays an important role in determining the predisposition for C—C bond formation to occur through either an inner- or outer-sphere process. As previously mentioned, decarboxylations via **TS5**, **TS14**, and **TS15** yield palladium enolates **(*Re*)-13**, **(*Si*)-13**, and **14**, respectively. From **(*Re/Si*)-13**, direct C—C bond formation through the inner-sphere transition states **(*Si*/chair)-TS20** or **(*Re*/boat)-TS20** represents the lowest energy pathway to the product. From **(*Re/Si*)-13**, the apparent barrier height to C—C bond formation via an outer-sphere mechanism corresponds to the isomerization of **(*Re/Si*)-13** to the axially bound enolate **14** via **(*Re/Si*)-TS21**, as ***Re/Si*)-TS21** are found to be higher in energy than the outer-sphere C—C bond forming transition states (**TS22**).

Therefore, decarboxylation through **TS5** or **TS14** (pathway 1 or 2) to directly afford **(Re/*Si*)-13** carries a predisposition for inner-sphere C—C bond formation.

Alternatively, decarboxylation via **TS15** (pathways 3) directly leads to apical enolate **14**. When this is the case, C—C bond formation through both inner- and outer-sphere processes becomes highly competitive. From **14**, the highest barrier to the outer-sphere mechanism is

Author Manuscript

Author Manuscript

Author Manuscript

Author Manuscript

that of the outer-sphere C—C bond forming event (**TS22**). While the barrier heights for the inner-sphere C—C bond forming transition states are lower in energy than those of the outer-sphere mechanism, the palladium enolate must first undergo an isomerization from apically bound **14** to square planar complexes **(*Re/Si*)-13**. In fact, the barrier heights of these isomerizations (via **(*Re/Si*)-TS21**) are comparable to that of the outer-sphere C—C bond formation. Therefore, less preference for the inner- over outer-sphere mechanism is expected for the case in which decarboxylation proceeds through **TS15** (pathway 3). Qualitatively similar results are obtained across a variety of density functional methods (see SI).

> We previously discussed the effects of solvation on the differentiation between decarboxylative pathways. We find that nonpolar solvents such as toluene impose a large preference for decarboxylation through the less polar **TS14**, while polar solvents result in preference for the more charge-separated **TS15**. Given the similarities in the free energies of the inner- and outer-sphere mechanisms, along with the experimentally observed solvent dependencies described in the literature, an analogous investigation into the solvent effects on differentiation of the inner- and outer-sphere mechanistic pathways was carried out.

First, we note the relative free energies between the low energy palladium enolates **(*Re/Si*)-13** and the transition states for their isomerization to **14** are independent of the continuum dielectric constant (Table 1). However, the barrier for C—C bond formation via inner-sphere **TS20** demonstrates a dependence on solvent polarity in which less polar solvents afford reduced barrier heights. As anticipated, the generation of solvent separated ions **15** and enolate **17** from **14** becomes increasingly unfavorable with decreasing dielectric constant of the solvent. As the relative free energy of **15** and **17** increases dramatically in nonpolar solvents, the outer-sphere C—C bond formation from the separate ions via **TS22** is anticipated to become less prevalent. In contrast, solvation in a continuum with a high dielectric constant favors the separate ions **15** and **17** over palladium enolate **14**. The barriers to outer-sphere C—C bond formation also decrease, now favoring an outer-sphere mechanism from **14**.

Taken together with the results for solvent effects on decarboxylation, we conclude that in polar solvent, decarboxylation via **TS15** is favored, affording intermediate **14**. From **14**, the minimum energy pathway to C—C bond formation is via a less enantioselective outer-sphere mechanism (**TS22**). Conversely, nonpolar solvents favor loss of CO_2 through **TS14**, yielding enolate **(*Si*)-13**. Reductive elimination via the 7-membered pericyclic transition state **TS20** then ensues. Given the sensitivity of relative barrier heights to changes in solvation, we highlight the need to consider both the mechanism of decarboxylation and that of the C—C bond forming pathways in determining the inner-sphere or outer-sphere mechanism to be more favorable.

Complete Catalytic Cycle.

Considering the findings for each step of the decarboxylative allylic alkylation reaction, we now construct a mechanistic picture that unites theoretical and experimental findings (Figure 12). First, the π-basic Pd^0(PHOX) precatalyst coordinates to the olefin of the allyl β-ketoester starting material (**1**), followed by net oxidative addition to form the [Pd(PHOx)(η^3-

Author Manuscript

Author Manuscript

Author Manuscript

Author Manuscript

allyl)]$^+$(RCO_2^-) ion pair (**4**). Oxidative addition occurs *trans* to the nitrogen of the PHOX ligand via direct displacement of the carboxylate leaving group (**TS4**). Validation of this displacement-type mechanism supports the basis from which previous claims have been made using inversion/retention of stereochemistry as a probe for determination of inner- versus outer-sphere mechanisms (when substitution on the allyl terminus is present).[6,27] The mechanism of Bäckvall was found to be unlikely for these substrates.[30] Furthermore, both enantiomers of the starting material have similar barriers to oxidative addition. This is in accordance with experimental evidence that a kinetic resolution of the allyl β-ketoester starting material is generally not observed.

Ion pair **4** then equilibrates to the more thermodynamically stable [Pd(PHOX)(η^1-allyl)(RCO_2)] complex (**3**) via a stepwise mechanism (Scheme 1). Experiment and computation agree in identifying **3** as the resting state of the catalyst. We further extend the analogous comparison to that of the enol carbonate substrate class (**8/9**). Given the equilibration between **3** and **4**, along with the similar relative energies of the separated ions, **we conclude that observation of crossover products in deuterium labeling experiments does not necessarily indicate an outer-sphere C—C bond forming mechanism but rather is still accommodated within the inner-sphere mechanistic hypothesis**.[5] That is, charge-separated ion pairs may undergo facile anion exchange to afford the observed cross products. Additionally, the pK_b of the carboxylate/carbonate anions is such that quenching with water to render an inactive or decomposed species is not anticipated, in accordance with the observed water tolerance experiments.[4]

Subsequent loss of CO_2 occurs through one (or more) of three unique decarboxylative transition states, each leading to a different palladium enolate intermediate. Our investigation determines that ion pair **4** (the initial product of oxidative addition) is a common intermediate along the two lowest energy pathways through decarboxylation. Therefore, the catalyst resting state (**3**) is best described as an off-cycle intermediate (Figure 13). In agreement with experiment, decarboxylation is determined here to be rate-limiting. Furthermore, the calculated rate of decarboxylation (4.65×10^{-4} s^{-1}) is in excellent agreement with that of experiment (1.58×10^{-4} s^{-1})[4].

From the four-coordinate palladium enolates **(*Re/Si*)-13**, the most facile pathway to C—C bond formation is inner-sphere reductive elimination via a 7-membered pericyclic transition state **(TS20). We establish that this C—C bond forming event is the enantiodetermining step**. Calculated enantioselectivities agree with the experiment and are assessed across a variety of computational methods. We propose a model for the origin of enantioinduction (Figure 11).

We investigated the interplay of inner- and outer-sphere mechanisms. In particular, we assess effects of solvation on the differentiation of these two processes. The highly enantioselective inner-sphere process is favored in nonpolar solvents, whereas the less selective outer-sphere mechanisms become increasingly relevant in polar solvents. The origin of this solvent dependence is 2-fold. In addition to stabilization of charged intermediates encountered in the outer-sphere processes, we find that increasingly polar solvents favor decarboxylation via the formally charge-separated transition state **TS15**, leading directly to the square pyramidal

Author Manuscript Author Manuscript Author Manuscript Author Manuscript

enolate complex **14**. Above, we discuss the implications of this in the context of a more facile entry into the outer-sphere mechanistic space.

EXPERIMENT AND DISCUSSION

We then sought to experimentally evaluate the mechanistic predictions obtained through our computational investigation. In the case of *α*-methyl allyl enol carbonate **8**, prior research reveals that the reaction rate is dramatically increased with the use of the more electron poor (*S*)-$(CF_3)_3$-*t*-BuPHOX ligand.[38] While a similar trend for the analogous *β*-ketoester (**1**) may be anticipated, reaction time course studies reveal that the same rate enhancement is not observed (Figure 14). In fact, when the catalyst resting state (**3**) and both low energy transition states responsible for decarboxylation (**TS14** and **TS15**) are reoptimized with the (*S*)-$(CF_3)_3$-*t*-BuPHOX ligand, the barrier to decarboxylation is calculated to be 22.2 kcal/mol (DLPNO-CCSD(T), TightPNO): nearly identical to the 21.9 kcal/mol (DLPNO-CCSD(T), TightPNO) barrier height of the original system. This experiment further highlights the fidelity of the computational methods employed in this study in describing the reactivity trends in the catalytic system.

We prepared *α*-phenyl allyl *β*-ketoester substrate **20** to probe the interplay of inner- and outer-sphere processes (Figure 15). In comparison to *α*-methylated *β*-ketoester **1**, the enolate derived from **20** experiences significant electronic stabilization through conjugation. As anticipated from the discussion provided above, as well as prior experimental trends, substrate **20** affords the desired product **(*S*)-22** in 99% yield, however, in a modest 23% ee.

It is worth noting that the reduction in enantioselectivity is likely not exclusively a consequence of steric interactions. A variety of sterically encumbered substrates, which do not provide significant electronic stabilization, such as the analogous *α*-*t*-Bu, *α*-Bn, *α*-prenyl, etc., compounds afford the corresponding allylic alkylation products in 82–91% ee.[5,31] Furthermore, we compute a $\Delta\Delta G^{\ddagger}$ of 1.3 kcal/mol between the enantiodetermining inner-sphere transition states derived from substrate **20** (corresponding to 80% ee at 25 °C). These results suggest that an enantioselective inner-sphere pathway persists; however, under the standard reaction conditions, the less selective outer-sphere mechanisms dominate.

In addition to *α*-phenyl *β*-ketoester **20**, the corresponding *α*-phenyl allyl enol carbonate synthon (**21**) was also evaluated in the transformation (Figure 15). Interestingly, under identical conditions to those employed with *β*-ketoester **20**, enol carbonate **21** affords **(*S*)-22** in a reduced 15% ee, compared to 23% ee as obtained starting from **20**.[8] After decarboxylation, both **20** and **21** share access to the same network of enolate intermediates (Scheme 2). By virtue of the differing mechanisms of decarboxylation, however, the point at which the intermediates derived from each substrate enter the postdecarboxylation mechanistic space is anticipated to vary. As prefaced by our computational investigation, this may lead to altered levels of product enantioenrichment due to the resulting predisposition for C—C bond formation to occur via inner- or outer-sphere mechanisms to varying extent (vida supra). Naturally, differences in enantioselectivities based on enolate synthon (i.e., *β*-ketoester versus enol carbonate) are expected to be increasingly pronounced in the case of stabilized enolates (**20**/**21**), for which an outer-sphere mechanism is readily accessible.

Author Manuscript Author Manuscript Author Manuscript Author Manuscript

These results highlight the importance in considering the effect of the mechanism of decarboxylation and subsequent behavior of enolate intermediates in the overall enantioselectivity of the transformation.

With compound **20** in hand, we then sought to probe the effects of solvation and ligand electronics on observed enantioselectivity (Table 2). As previously mentioned, the enantioselective inner-sphere pathway to C—C bond formation to **(*S*)-22** is expected to be largely outcompeted by less selective outer-sphere mechanisms. Our computational investigations suggest that for allyl β-ketoesters, inner-sphere mechanisms are favored by (1) disfavoring the charge-separated intermediates required for an outer-sphere approach and (2) favoring decarboxylative mechanisms that lead directly to η^1-allyl square planar palladium enolates (i.e., via decarboxylation pathways 1 and 2). Calculations further predicted that this may be accomplished by utilizing nonpolar solvents, as well as through the installation of electron withdrawing groups on the PHOX ligand framework.

Indeed, we observe an increase from 23 to 28% ee simply by implementing toluene ($\varepsilon = 2.4$) in place of THF ($\varepsilon = 7.3$) as the reaction solvent (entries 1–2, Table 2). Utilizing the more electron poor (*S*)-$(CF_3)_3$-*t*-BuPHOX ligand in toluene (entry 3) and a 2:1 methylcyclohexane/toluene solvent mixture ($\varepsilon = 2.1$), enantioselectivity was further enhanced to 32% and 36% ee, respectively (entries 3–4). Given the initial improvements from perturbations of ligand electronics and solvation alone, we suggest in silico high-throughput screening of ligands with different steric environments as a practical next step in future developmental efforts.

CONCLUSIONS

We report a detailed quantum mechanics investigation into the three mechanistic steps (oxidative addition, decarboxylation, and reductive elimination) of the decarboxylative asymmetric allylic alkylation with the Pd(PHOX) catalyst system. Experiments were carried out to explore the mechanistic hypotheses derived from the ab initio calculations.

Beginning with allyl β-ketoester **1**, oxidative addition of Pd^0(PHOX) proceeds through precoordination of the olefin of the allyl fragment of **1** (to give **5**), followed by an S_N2-like electrophilic addition to Pd to yield the $[(PHOX)Pd(\eta^3\text{-allyl})]^+(RCO_2^-)$ ion pair (**4**). Ion pair **4** then rapidly equilibrates to the catalyst resting state, $[(PHOX)Pd(\eta^1\text{-allyl})(RCO_2)]$ (**3**). Complex **3** is best described as an off-cycle intermediate. Given the equilibration between **3** and **4**, along with the similar relative energies of the separated ions, **we corroborate that the results from our previously reported crossover experiments are not necessarily indicative of an outer-sphere mechanism but still are accommodated within the inner-sphere mechanistic hypothesis.**

From the catalyst resting state (**3**), we find three dominant pathways (1, 2, and 3) through which decarboxylation may occur. Each pathway leads to a unique palladium enolate with the ability for subsequent interconversion between the three. However, the ensuing analysis of the C—C bond forming potential energy surface reveals that the enolates derived from pathways 1 and 2 are more predisposed to undergo an inner-sphere C—C bond formation

Author Manuscript

Author Manuscript

Author Manuscript

Author Manuscript

via the 7-membered pericyclic transition state, **TS20**. Decarboxylation via pathway 3 directly affords square pyramidal enolate **14** which may undergo a more facile dissociation and enter the outer-sphere mechanistic space.

We predict relative barrier heights among the decarboxylative and C(sp^3)–C(sp^3) bond forming pathways to be highly solvent dependent. **Decreasing solvent polarity favors inner-sphere processes by destabilizing the ionic intermediates of the outer-sphere mechanism as well as promoting decarboxylation via pathway 2.** Decarboxylation is determined to be rate-limiting in accordance with experiment. Furthermore, the calculated decarboxylation rate constant in THF obtained with DLPNO-CCSD(T) (4.65×10^{-4} s^{-1}, $\Delta G^{\ddagger} = 22.0$ kcal/mol) is in excellent agreement with that of experiment (1.58×10^{-4} s^{-1}, $\Delta G^{\ddagger} = 22.6$ kcal/mol).[4] In comparison, the DFT methods applied in this study all predict a rate constant 10^3–10^7 times larger in magnitude ($\Delta G^{\ddagger} = 12.5$–$18.9$ kcal/mol) than that experimentally observed.

We considered several inner-sphere reductive elimination transition states. In accordance with previous research in our group, the 7-membered, doubly vinylogous transition state (**TS20**)[39] provides the lowest energy pathway to C—C bond formation in nonpolar solvents. **We establish that the C(sp^3)–C(sp^3) bond forming event is the enantiodetermining step**. Calculated $\Delta\Delta G^{\ddagger}$ are in excellent agreement with experimentally observed enantioselectivities and are assessed across a variety of computational methods.[40] A model is proposed for the origin of the enantioinduction.

We also investigated outer-sphere processes, which we found to be competitive in barrier height with the inner-sphere reactions, albeit slightly less favorable. Unlike the inner-sphere transition states, however, **severely degraded enantiocontrol is anticipated for outer sphere mechanisms.**

Additionally, enolate synthon design is highlighted as an area for future development. Herein, we compare the relative thermodynamics of catalyst resting states derived from different enolate precursors. From this, we suggest that in conjunction with catalyst design, **the development of more activated masked enolates may achieve a desirable increase in reaction rate.** With a complete mechanistic picture in hand, in silico development may now accompany ensuing experimental efforts.

In order to evaluate the fidelity of the mechanistic hypotheses, a stabilized enolate equivalent (**20**) was employed as a probe for inner- and outer-sphere competition. Experimental results support the computation-based predictions in solvent trends as well as effects of ligand substitution. Furthermore, a comparison between **20** and **21** demonstrates the intricacies in the equilibration of the palladium enolate intermediates as described herein. While α-methyl ketone **1** is employed throughout the majority of this study as a “standard” substrate, many of the experimentally observed trends mentioned throughout the text remain consistent among more highly decorated heterocyclic scaffolds alike. Thus, the conclusions presented herein are expected to serve as robust first-order approximations to a broad variety of substrate classes.

Density functional theory and localized coupled-cluster theory are employed in this study. We find the DLPNO-CCSD(T) method of Neese et al. highly effective in obtaining accurate barrier heights and thermodynamic relations.[24] **Thus, we recommend DLPNO-CCSD(T) for routine use in future quantum mechanics-based investigations in asymmetric catalysis.**

These avenues of thought, coupled with the detailed mechanistic hypothesis presented herein, provide a powerful tool in addressing current limitations and aiding in the future development of the decarboxylative asymmetric allylic alkylation reaction.

Supplementary Material

Refer to Web version on PubMed Central for supplementary material.

ACKNOWLEDGMENTS

We thank the NIH (R01 GM080269) and Caltech for financial support. We further thank Dr. Michael Bartberger (1200 Pharma) for insightful discussion. W.A.G. received support from ONR (ONR N00014-18-1-2155). The Caltech High Performance Computing (HPC) center is acknowledged for support of computational resources.

REFERENCES

(1) (a). Trost BM; Jiang C Catalytic Enantioselective Construction of All-Carbon Quaternary Stereocenters. Synthesis 2006, 3, 369–396.(b)Corey EJ; Guzman-Perez A The Catalytic Enantioselective Construction of Molecules with Quaternary Carbon Stereocenters. Angew. Chem., Int Ed 1998, 37, 388–401.

(2). Liu Y; Han S-J; Liu W-B; Stoltz BM Catalytic Enantioselective Construction of Quaternary Stereocenters: Assembly of Key Building Blocks for the Synthesis of Biologically Active Molecules. Acc. Chem. Res 2015, 48, 740–751. [PubMed: 25715056]

(3). Behenna DC; Mohr JT; Sherden NH; Marinescu SC; Harned AM; Tani K; Seto M; Ma S; Novák Z; Krout MR; McFadden RM; Roizen JL; Enquist JA; White DE; Levine SR; Petrova KV; Iwashita A; Virgil SC; Stoltz BM Enantioselective Decarboxylative Alkylation Reactions: Catalyst Development, Substrate Scope, and Mechanistic Studies. Chem. - Eur. J 2011, 17, 14199–14223. [PubMed: 22083969]

(4). Note that product enantioenrichment follows a linear correlation with PHOX ligand enantioenrichment. Sherden NH; Behenna DC; Virgil SC; Stoltz BM Unusual Allylpalladium Carboxylate Complexes: Identification of the Resting State of Catalytic Enantioselective Decarboxylative Allylic Alkylation Reactions of Ketones. Angew. Chem., Int. Ed 2009, 48, 6840–6843.

(5). Mohr JT; Behenna DC; Harned AM; Stoltz BM Deracemization of Quaternary Stereocenters by Pd-Catalyzed Enantioconvergent Decarboxylative Allylation of Racemic β-Ketoesters. Angew. Chem. Int. Ed 2005, 44, 6924–6927.

(6). Trost BM; Xu J; Schmidt T Palladium-Catalyzed Decarboxylative Asymmetric Allylic Alkylation of Enol Carbonates. J. Am. Chem. Soc 2009, 131, 18343–18357. [PubMed: 19928805]

(7). For review of classes of nucleophiles as well as mechanistic implications: (a) Trost BM; Crawley ML Asymmetric Transition-Metal-Catalyzed Allylic Alkylations: Applications in Total Synthesis. Chem. Rev 2003, 103, 2921–2944 Highlighting the challenge of employing “hard” ketone enolate nucleophiles:. [PubMed: 12914486] (b)Trost BM; Schroeder GM Palladium-Catalyzed Asymmetric Alkylation of Ketone Enolates. J. Am. Chem. Soc 1999, 121, 6759–6760 For examples of stabilized ketone enolates with Trost system:.(c)Trost BM; Schroeder GM; Kristensen J Palladium-Catalyzed Asymmetric Allylic Alkylation of α-Aryl Ketones. Angew. Chem., Int. Ed 2002, 41, 3492–3495.(d)Trost BM; Radinov R; Grenzer EM Asymmetric Alkylation of β-Ketoesters. J. Am. Chem. Soc 1997, 119, 7879–7880.

Author Manuscript Author Manuscript Author Manuscript Author Manuscript

(8). McDougal NT; Virgil SC; Stoltz BM High-Throughput Screening of the Asymmetric Decarboxylative Alkylation Reaction of Enolate-Stabilized Enol Carbonates. Synlett 2010, 11, 1712–1716. [PubMed: 21072327]

(9) (a). Sun AW; Hess SN; Stoltz BM Enantioselective Synthesis of Gem-Disubstituted N-Boc Diazaheterocycles via Decarboxylative Asymmetric Allylic Alkylation. Chem. Sci 2019, 10, 788–792. [PubMed: 30774872] (b)Sun AW; Bulterys PL; Bartberger MD; Jorth PA; O'Boyle BM; Virgil SC; Miller JF; Stoltz BM Incorporation of a Chiral Gem-Disubstituted Nitrogen Heterocycle Yields an Oxazolidinone Antibiotic with Reduced Mitochondrial Toxicity. Bioorg. Med. Chem. Lett 2019, 29, 2686–2689. [PubMed: 31383589] (c)Numajiri Y; Jiménez-Osés G; Wang B; Houk KN; Stoltz BM Enantioselective Synthesis of Dialkylated N-Heterocycles by Palladium-Catalyzed Allylic Alkylation. Org. Lett 2015, 17, 1082–1085. [PubMed: 25714704] (d)Behenna DC; Liu Y; Yurino T; Kim J; White DE; Virgil SC; Stoltz BM Enantioselective Construction of Quaternary N-Heterocycles by Palladium-Catalysed Decarboxylative Allylic Alkylation of Lactams. Nat. Chem 2012, 4, 130–133.(e)Bennett NB; Duquette DC; Kim J; Liu W-B; Marziale AN; Behenna DC; Virgil SC; Stoltz BM Expanding Insight into Asymmetric Palladium-Catalyzed Allylic Alkylation of N-Heterocyclic Molecules and Cyclic Ketones. Chem. - Eur. J 2013, 19, 4414–4418. [PubMed: 23447555] (f)Korch KM; Eidamshaus C; Behenna DC; Nam S; Horne D; Stoltz BM Enantioselective Synthesis of α-Secondary and α-Tertiary Piperazin-2-Ones and Piperazines by Catalytic Asymmetric Allylic Alkylation. Angew. Chem., Int. Ed 2015, 54, 179–183.

(10) (a). Keith JA; Behenna DC; Mohr JT; Ma S; Marinescu SC; Oxgaard J; Stoltz BM; Goddard WA The Inner-Sphere Process in the Enantioselective Tsuji Allylation Reaction with (S)-t-Bu-Phosphinooxazoline Ligands. J. Am. Chem. Soc 2007, 129, 11876–11877. [PubMed: 17824701] (b)Keith JA; Behenna DC; Sherden N; Mohr JT; Ma S; Marinescu SC; Nielsen RJ; Oxgaard J; Stoltz BM; Goddard WA The Reaction Mechanism of the Enantioselective Tsuji Allylation: Inner-Sphere and Outer-Sphere Pathways, Internal Rearrangements, and Asymmetric C—C Bond Formation. J. Am. Chem. Soc 2012, 134, 19050–19060. [PubMed: 23102088]

(11) (a). Neese F Software Update: The ORCA Program System, Version 4.0. Wiley Interdiscip. Rev.: Comput. Mol. Sci 2018, 8, e1327.(b)Neese F The ORCA Program System. Wiley Interdiscip. Rev.: Comput. Mol. Sci 2012, 2, 73–78.

(12) (a). Perdew JP Density-Functional Approximation for the Correlation Energy of the Inhomogeneous Electron Gas. Phys. Rev. B: Condens. Matter Mater. Phys 1986, 33, 8822–8824. (b)Becke AD Density-Functional Exchange-Energy Approximation with Correct Asymptotic Behavior. Phys. Rev. A: At., Mol., Opt. Phys 1988, 38, 3098–3100.

(13) (a). Grimme S; Antony J; Ehrlich S; Krieg H A A consistent and accurate ab initio parametrization of density functional dispersion correction (DFT-D) for the 94 elements H-Pu. J. Chem. Phys 2010, 132 (15), 154104. [PubMed: 20423165] (b)Grimme S; Ehrlich S; Goerigk L Effect of the Damping Function in Dispersion Corrected Density Functional Theory. J. Comput. Chem 2011, 32, 1456–1465. [PubMed: 21370243] (c)Becke AD; Johnson ERA density-functional model of the dispersion interaction. J. Chem. Phys 2005, 122, 154101. [PubMed: 15945619] (d)Johnson ER; Becke AD A post-Hartree–Fock model of intermolecular interactions. J. Chem. Phys 2005, 123, 024101.(e)Johnson ER; Becke AD A post-Hartree- Fock model of intermolecular interactions: Inclusion of higher-order corrections. J. Chem. Phys 2006, 124, 174104. [PubMed: 16689564]

(14). Hay PJ; Wadt WR Ab Initio Effective Core Potentials for Molecular Calculations. Potentials for the Transition Metal Atoms Sc to Hg. J. Chem. Phys 1985, 82, 270–283.

(15). Stephens PJ; Devlin FJ; Chabalowski CF; Frisch MJ Ab Initio Calculation of Vibrational Absorption and Circular Dichroism Spectra Using Density Functional Force Fields. J. Phys. Chem 1994, 98, 11623–11627.

(16). Adamo C; Barone V Toward Reliable Density Functional Methods without Adjustable Parameters: The PBE0Model. J. Chem. Phys 1999, 110, 6158–6170.

(17). Zhao Y; Truhlar DG The M06 Suite of Density Functionals for Main Group Thermochemistry, Thermochemical Kinetics, Non-covalent Interactions, Excited States, and Transition Elements: Two New Functionals and Systematic Testing of Four M06-Class Functionals and 12 Other Functionals. Theor. Chem. Acc 2008, 120, 215–241.

Author Manuscript

Author Manuscript

Author Manuscript

Author Manuscript

(18). Kozuch S; Gruzman D; Martin JML DSD-BLYP: A General Purpose Double Hybrid Density Functional Including Spin Component Scaling and Dispersion Correction. J. Phys. Chem. C 2010, 114, 20801–20808.

(19). Weigend F; Ahlrichs R Balanced Basis Sets of Split Valence, Triple Zeta Valence and Quadruple Zeta Valence Quality for H to Rn: Design and Assessment of Accuracy. Phys. Chem. Chem. Phys 2005, 7 (18), 3297–3305. [PubMed: 16240044]

(20). Andrae D; Häußermann U; Dolg M; Stoll H; Preuß H Energy-Adjusted ab Initio Pseudopotentials for the Second and Third Row Transition Elements. Theoret. Chim. Acta 1990, 77 (2), 123–141.

(21). Barone V; Cossi M Quantum Calculation of Molecular Energies and Energy Gradients in Solution by a Conductor Solvent Model. J. Phys. Chem. A 1998, 102, 1995–2001.

(22). Grimme S Supramolecular Binding Thermodynamics by Dispersion-Corrected Density Functional Theory. Chem. - Eur. J 2012, 18, 9955–9964. [PubMed: 22782805]

(23). Legault CY CYLView, 1.0b; Universite´ de Sherbrooke, Canada, 2009; http://www.cylview.org.Note that solvent exposed surface plots were generated with Chimera:. Pettersen EF; Goddard TD; Huang CC; Couch GS; Greenblatt DM; Meng EC; Ferrin TE UCSF Chimera – a visualization system for exploratory research and analysis. J. Comput. Chem 2004, 25, 1605–1612. [PubMed: 15264254]

(24) (a). Riplinger C; Neese F An Efficient and near Linear Scaling Pair Natural Orbital Based Local Coupled Cluster Method. J. Chem. Phys 2013, 138 (3), 034106. [PubMed: 23343267] (b)Riplinger C; Sandhoefer B; Hansen A; Neese F Natural Triple Excitations in Local Coupled Cluster Calculations with Pair Natural Orbitals. J. Chem. Phys 2013, 139 (13), 134101. [PubMed: 24116546] (c)Riplinger C; Pinski P; Becker U; Valeev EF; Neese F Sparse Maps—A Systematic Infrastructure for Reduced-Scaling Electronic Structure Methods. II. Linear Scaling Domain Based Pair Natural Orbital Coupled Cluster Theory. J. Chem. Phys 2016, 144 (2), 024109. [PubMed: 26772556]

(25). Peterson KA; Figgen D; Dolg M; Stoll H Energy-Consistent Relativistic Pseudopotentials and Correlation Consistent Basis Sets for the 4d Elements Y–Pd. J. Chem. Phys 2007, 126, 124101. [PubMed: 17411102]

(26) (a). Yamamoto T; Saito O; Yamamoto A Oxidative Addition of Allyl Acetate to Palladium(0) Complexes. J. Am. Chem. Soc 1981, 103, 5600–5602.(b)Yamamoto T; Akimoto M; Saito O; Yamamoto A Interaction of Palladium(0) Complexes with Allylic Acetates, Allyl Ethers, Allyl Phenyl Chalcogenides, Allylic Alcohols, and Allylamines. Oxidative Addition, Condensation, Disproportionation, and π-Complex Formation. OrganometaUics 1986, 5, 1559–1567. (c)Amatore C; Jutand A; Meyer G; Mottier L Evidence of the Reversible Formation of Cationic π-Allylpalladium(II) Complexes in the Oxidative Addition of Allylic Acetates to Palladium(0) Complexes. Chem. - Eur. J 1999, 5, 466–473.

(27). Trost BM; Verhoeven TR Allylic Substitutions with Retention of Stereochemistry. J. Org. Chem 1976, 41, 3215–3216.

(28). Ariafard A; Lin Z Understanding the Relative Easiness of Oxidative Addition of Aryl and Alkyl Halides to Palladium(0). Organometallics 2006, 25, 4030–4033.

(29). Low JJ; Goddard WA Theoretical Studies of Oxidative Addition and Reductive Elimination. 3. Carbon-Hydrogen and Carbon-Carbon Reductive Coupling from Palladium and Platinum Bis-(Phosphine) Complexes. J. Am. Chem. Soc 1986, 108 (20), 6115–6128.

(30). Grennberg H; Langer V; Bäckvall J-E Structure and Reactivity of Cis- and Trans-Bis-[{5-Carbomethoxy-(1,2,3-η)-Cyclohexenyl}palladium]. Evidence for a (σ-Allyl)Palladium Intermediate in the Cis-Migration of Acetate from Palladium to Coordinated π-Allyl. J. Chem. Soc., Chem. Commun 1991, 17, 1190–1192.

(31). Behenna DC; Stoltz BM The Enantioselective Tsuji Allylation. J. Am. Chem. Soc 2004, 126, 15044–15045. [PubMed: 15547998]

(32). Behenna DC Progress toward the synthesis of (+)-zoanthenol and the development of an asymmetric Tsuji allylation reaction Ph.D. Dissertation, California Institute of Technology, Pasadena, CA, 2007.

(33) (a). Pérez-Rodríguez M; Braga AAC; de Lera AR; Maseras F; Álvarez R; Espinet P A DFT Study of the Effect of the Ligands in the Reductive Elimination from Palladium Bis(Allyl) Complexes.

Author Manuscript

Author Manuscript

Author Manuscript

Author Manuscript

Organometallics 2010, 29 (21), 4983–4991.(b)Méndez M; Cuerva JM; Gómez-Bengoa E; Cárdenas DJ; Echavarren AM Intramolecular Coupling of Allyl Carboxylates with Allyl Stannanes and Allyl Silanes: A New Type of Reductive Elimination Reaction? Chem. - Eur. J 2002, 8 (16), 3620–3628. [PubMed: 12203288] (c)Zhang P; Brozek LA; Morken JP Pd-Catalyzed Enantioselective Allyl–Allyl Cross-Coupling. J. Am. Chem. Soc 2010, 132, 10686–10688. [PubMed: 20681700]

(34) (a). Trost BM; Thaisrivongs DA Strategy for Employing Unstabilized Nucleophiles in Palladium-Catalyzed Asymmetric Allylic Alkylations. J. Am. Chem. Soc 2008, 130, 14092–14093. [PubMed: 18826305] (b)Zhang K; Peng Q; Hou X-L; Wu Y-D Highly Enantioselective Palladium-Catalyzed Alkylation of Acyclic Amides. Angew. Chem. Int. Ed 2008, 47, 1741–1744. (c)Trost BM; Xu J; Schmidt T Palladium-Catalyzed Decarboxylative Asymmetric Allylic Alkylation of Enol Carbonates. J. Am. Chem. Soc 2009, 131, 18343–18357. [PubMed: 19928805]

(35) (a). Aranyos A; Szabó KJ; Castaño AM; Bäckvall J-E Central versus Terminal Attack in Nucleophilic Addition to (π-Allyl) Palladium Complexes. Ligand Effects and Mechanism. Organometallics 1997, 16, 1058–1064.(b)Szabó KJ Effects of the Ancillary Ligands on Palladium–Carbon Bonding in (η^3-Allyl)Palladium Complexes. Implications for Nucleophilic Attack at the Allylic Carbons. Organometallics 1996, 15, 1128–1133.(c)Castaño AM; Aranyos A; Szabó KJ; Bäckvall J-E Nucleophilic Attack on (π-Allyl)Palladium Complexes: Direction of the Attack to the Central or Terminal Carbon Atom by Ligand Control. Angew. Chem., Int. Ed. Engl 1995, 34, 2551–2553.

(36). Hegedus LS; Darlington WH; Russell CE Cyclopropanation of Ester Enolates by π-Allylpalladium Chloride Complexes. J. Org. Chem 1980, 45 (25), 5193–5196.

(37). Hoffmann HMR; Otte AR; Wilde A; Menzer S; Williams DJ Isolation and X-Ray Crystal Structure of a Palladacyclobutane: Insight into the Mechanism of Cyclopropanation. Angew. Chem., Int. Ed. Engl 1995, 34, 100–102.

(38). Tani K; Behenna DC; McFadden RM; Stoltz BM A Facile and Modular Synthesis of Phosphinooxazoline Ligands. Org. Lett 2007, 9 (13), 2529–2531. [PubMed: 17536810]

(39). Investigations into the electronic structure of the unique 7-membered transition state are ongoing and will be published in due course.

(40). Theoretical product enantioenrichments of 81% ee at the M06 level of theory is calculated with a Boltzman-weighted average of all eight unique inner-sphere transition states (experimental value of 88% ee). Likewise, a value of 94% ee is obtained with DLPNO-CCSD(T). Further calculations with the computationally more costly “TightPNO” settings are employed for the two lowest energy pair diastereomeric complexes, resulting in a calculated 92% ee.

Author Manuscript Author Manuscript Author Manuscript Author Manuscript

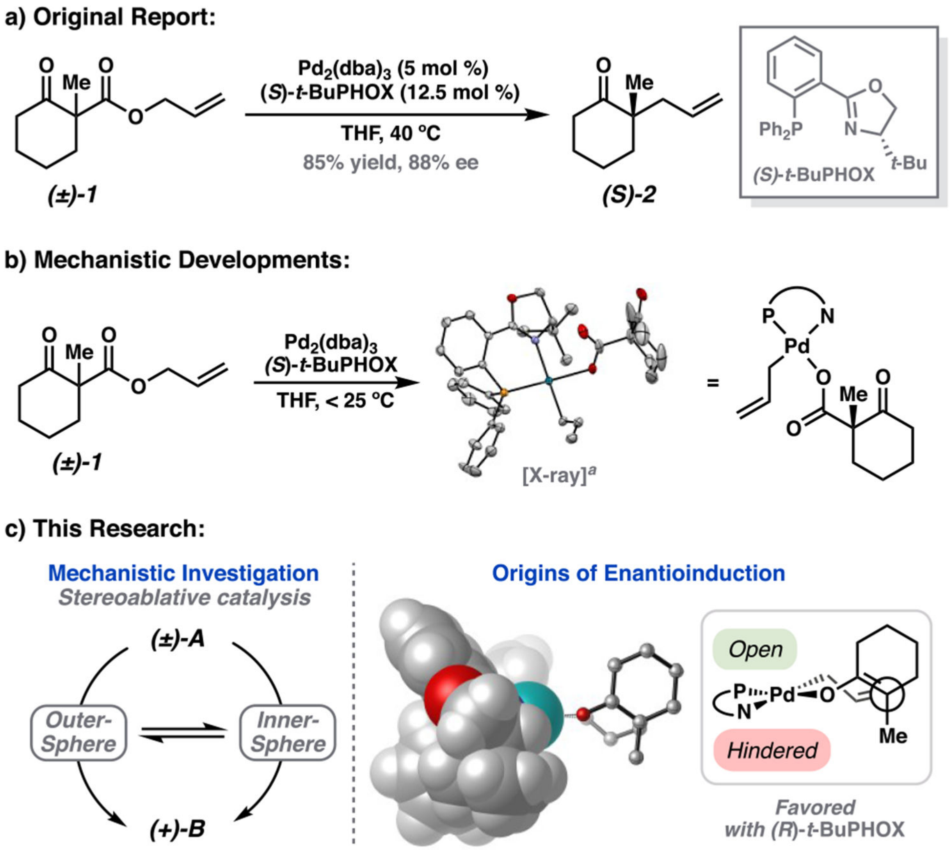

Figure 1.

Previous research by the Stoltz group. (a) Original report of allyl *β*-ketoester substrate class.[5] (b) Mechanistic developments.[4] [a]Crystal structure of the (*S*)-*t*-BuPHOX carboxylate complex (opposite enantiomer as used in this study). (c) Scope of this research.

Author Manuscript
Author Manuscript
Author Manuscript
Author Manuscript

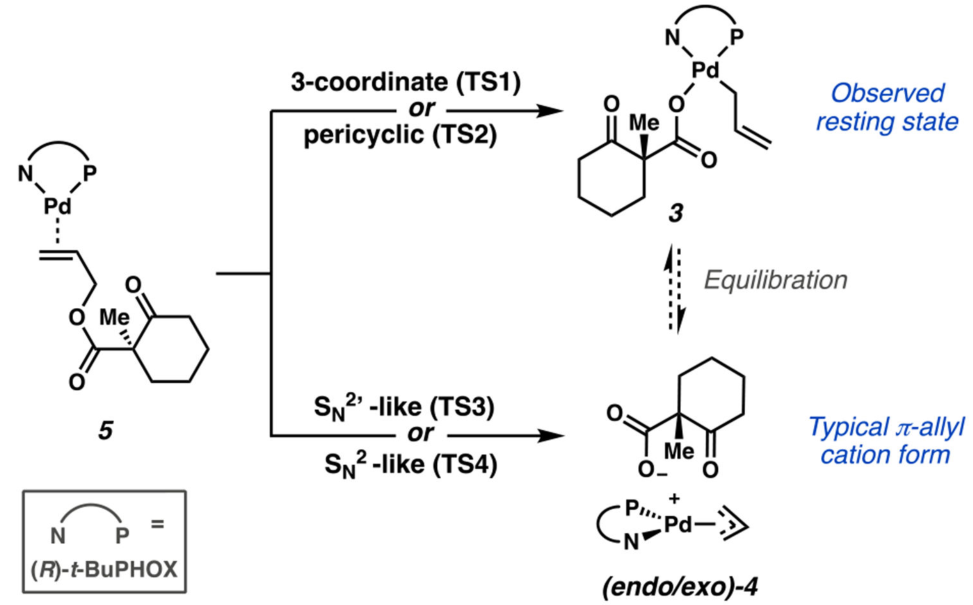

Figure 2.

Pathways considered for oxidative addition to either **3** or **4** from **5**.

Author Manuscript
Author Manuscript
Author Manuscript
Author Manuscript

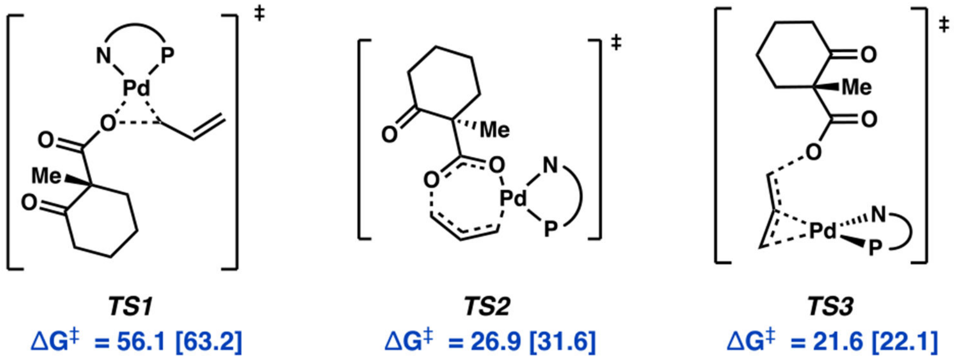

TS1 $\Delta G^{\ddagger}$ = 56.1 [63.2]

TS2 $\Delta G^{\ddagger}$ = 26.9 [31.6]

TS3 $\Delta G^{\ddagger}$ = 21.6 [22.1]

Figure 3.

Initial transition states considered for oxidative addition. Free energies (M06) given in kcal/mol with free energies calculated at the DLPNO-CCSD(T) level in brackets.

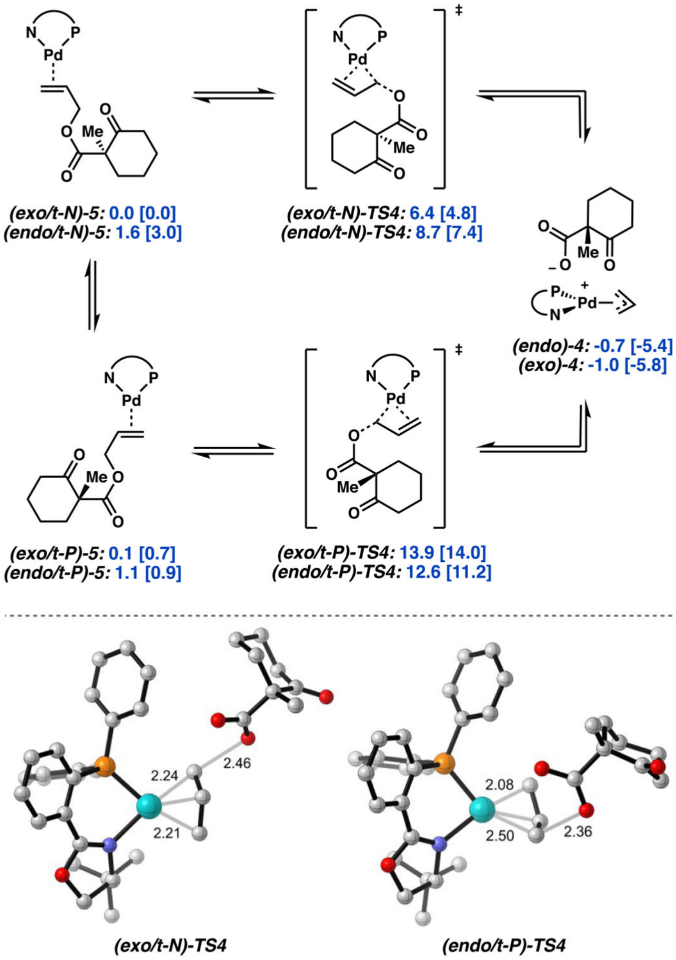

Figure 4.

Free energy network encompassing all four isomeric forms of **TS4**. Free energies (M06) given in kcal/mol with free energies calculated at the DLPNO-CCSD(T) level in brackets.

Author Manuscript Author Manuscript Author Manuscript Author Manuscript

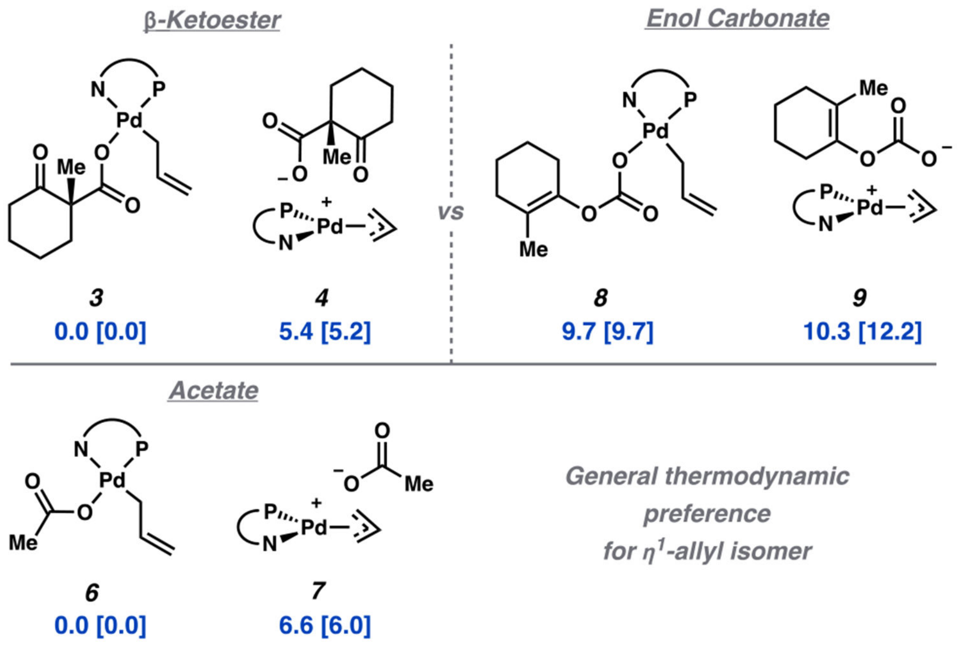

Figure 5.

Relative free energies (M06) in kcal/mol of constitutional isomers of η^1 and η^3-bound allyl palladium complexes with masked enolate synthons (top). Analogous case for complexes derived from allyl acetate (bottom). Free energies calculated at the DLPNO-CCSD(T) level in brackets.

Author Manuscript

Author Manuscript

Author Manuscript

Author Manuscript

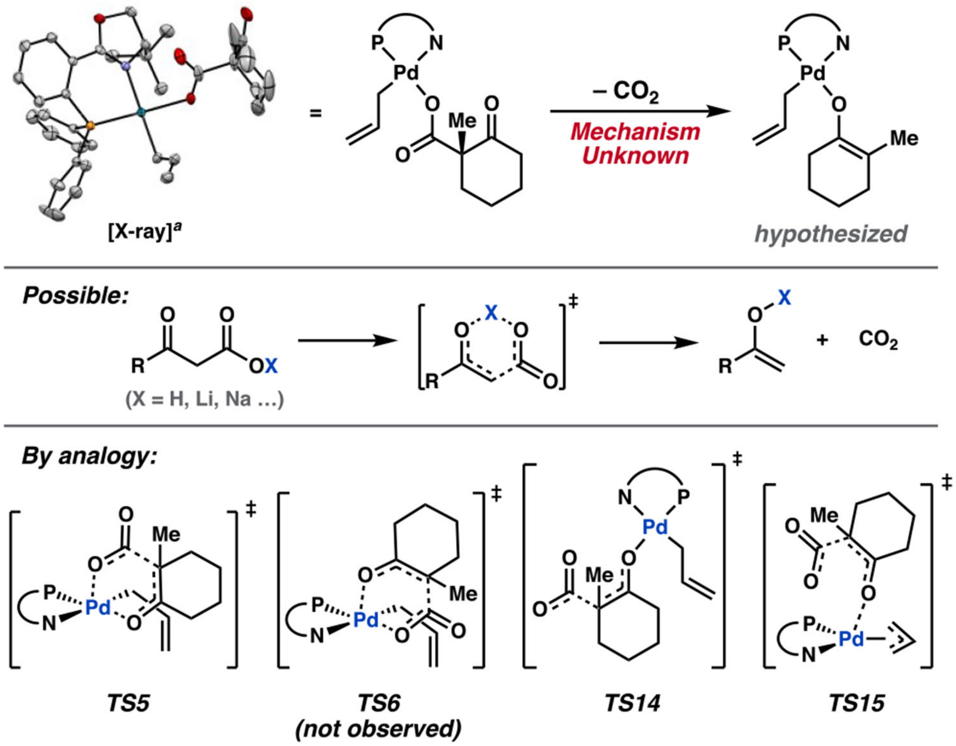

Figure 6.

Decarboxylative transition states considered herein. [a]X-ray structure of one diastereomer of **3** with 50% probability ellipsoids (opposite enantiomer of PHOX ligand used in this study).[4]

Author Manuscript Author Manuscript Author Manuscript Author Manuscript

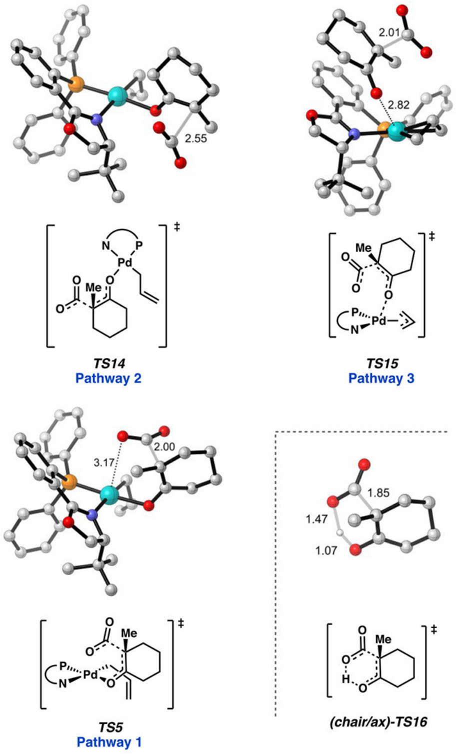

	Toluene (ε = 2.4)	Et$_2$O (ε = 4.3)	THF (ε = 7.3)	DMF (ε = 38.2)
TS14	15.4 (0.0)	16.5 (0.0)	17.1 (0.0)	17.9 (1.3)
TS15	19.6 (4.2)	18.3 (1.8)	17.5 (0.4)	16.6 (0.0)
TS5	21.9 (6.5)	22.0 (5.5)	22.0 (4.9)	22.0 (5.4)
TS16[e]	-	-	20.3[a] (3.1)	-

Figure 7.

Structures of rate-limiting transition states for decarboxylation pathways 1, 2, and 3 (top). Apparent barriers to decarboxylation ($\Delta G^{\ddagger}$ from **3**) with $\Delta G^{\ddagger}_{\mathrm{rel}}$ in parentheses (bottom). Free energies reported in kcal/mol, calculated with M06/def2-TZVP–CPCM-(*solvent*) on gas phase geometries. [a]With respect to the corresponding *β*-ketoacid (**16-H**).

Author Manuscript

Author Manuscript

Author Manuscript

Author Manuscript

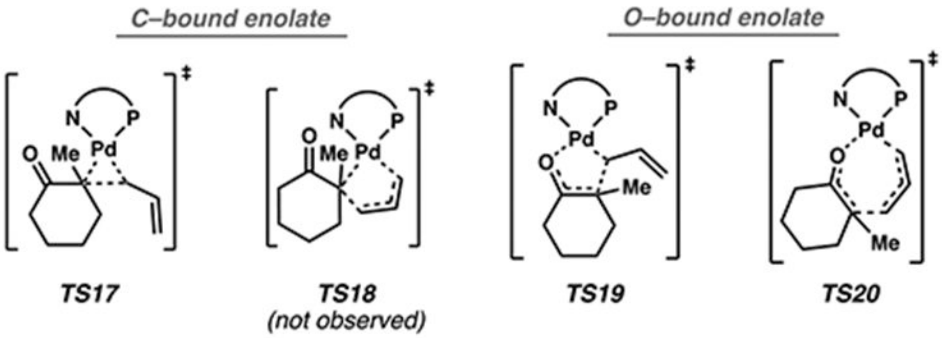

Figure 8.

Inner-sphere C(sp^3)–C(sp^3) bond forming transition states considered.

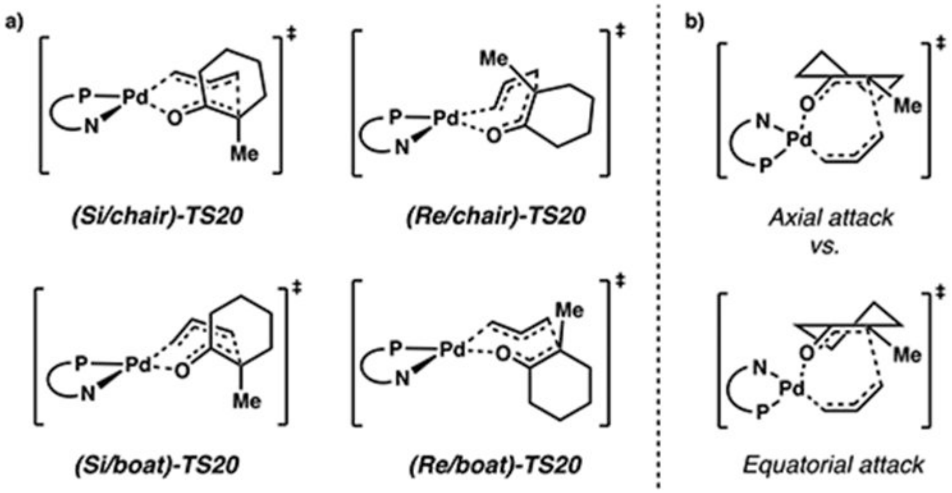

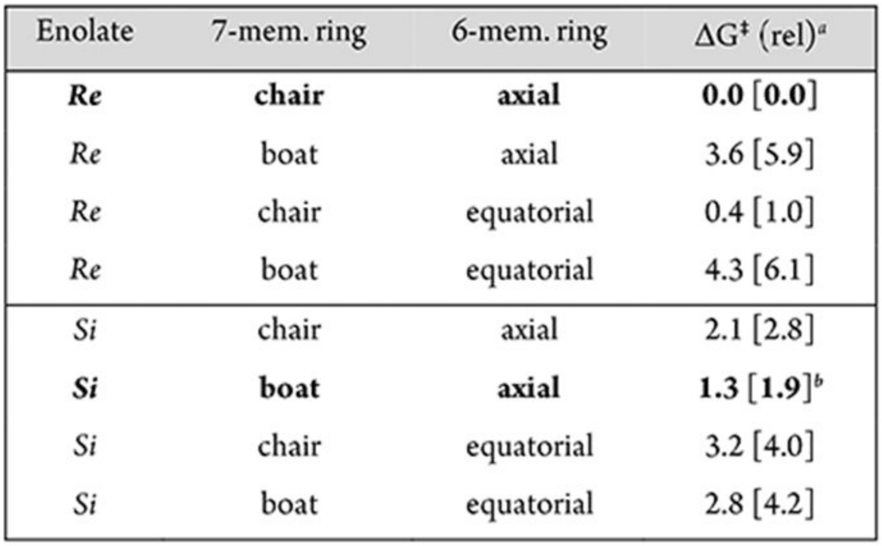

Enolate	7-mem. ring	6-mem. ring	ΔG‡ (rel)[a]
Re	**chair**	**axial**	**0.0 [0.0]**
Re	boat	axial	3.6 [5.9]
Re	chair	equatorial	0.4 [1.0]
Re	boat	equatorial	4.3 [6.1]
Si	chair	axial	2.1 [2.8]
Si	**boat**	**axial**	**1.3 [1.9]**[b]
Si	chair	equatorial	3.2 [4.0]
Si	boat	equatorial	2.8 [4.2]

Figure 9.

(a) Four conformational geometries of the seven-membered ring (top). (b) Two cyclic enolate half-chair conformers possible for each of the four conformers depicted in part a. Comparison of relative free energy barrier heights among eight 7-membered ring reductive elimination transition states (bottom; **TS20**). [a]Relative free energies given in kcal/mol at the M06/def2-TZVP–CPCM(THF) level of theory with DLPNO-CCSD(T)/cc-pVTZ–CPCM(THF) values in brackets. [b]With TightPNO settings.

Author Manuscript

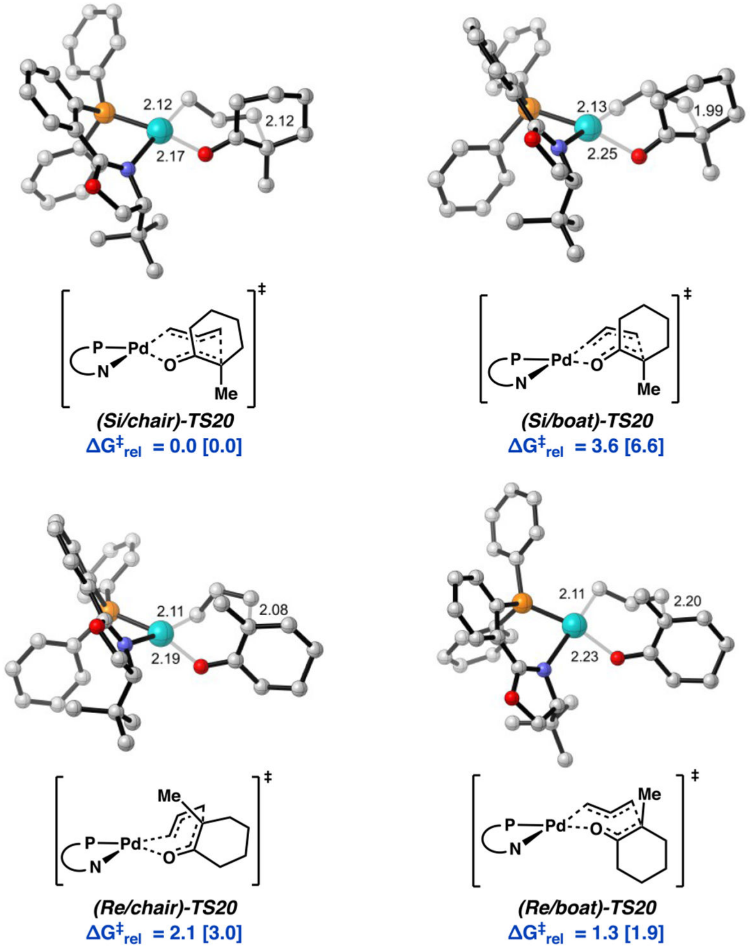

(Si/chair)-TS20 $\Delta G^{\ddagger}_{rel}$ = 0.0 [0.0]

(Si/boat)-TS20 $\Delta G^{\ddagger}_{rel}$ = 3.6 [6.6]

(Re/chair)-TS20 $\Delta G^{\ddagger}_{rel}$ = 2.1 [3.0]

(Re/boat)-TS20 $\Delta G^{\ddagger}_{rel}$ = 1.3 [1.9]

Figure 10.

Relative free energies of boat and chair conformers of (***Re***)- and **(*Si*)-TS20** obtained with M06/def2-TZVP–CPCM(THF), with energies at the DLPNO-CCSD(T)/cc-pVTZ–CPCM(THF) level of theory in brackets.

Author Manuscript
Author Manuscript
Author Manuscript
Author Manuscript

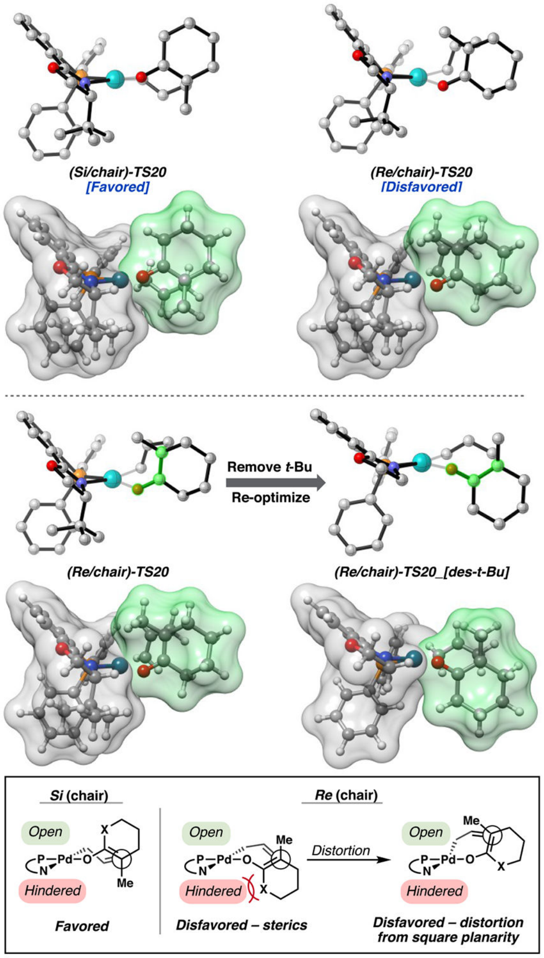

Figure 11.

Hypothesized mechanism of stereoinduction. Side on view of relevant transition states.

Author Manuscript Author Manuscript Author Manuscript Author Manuscript

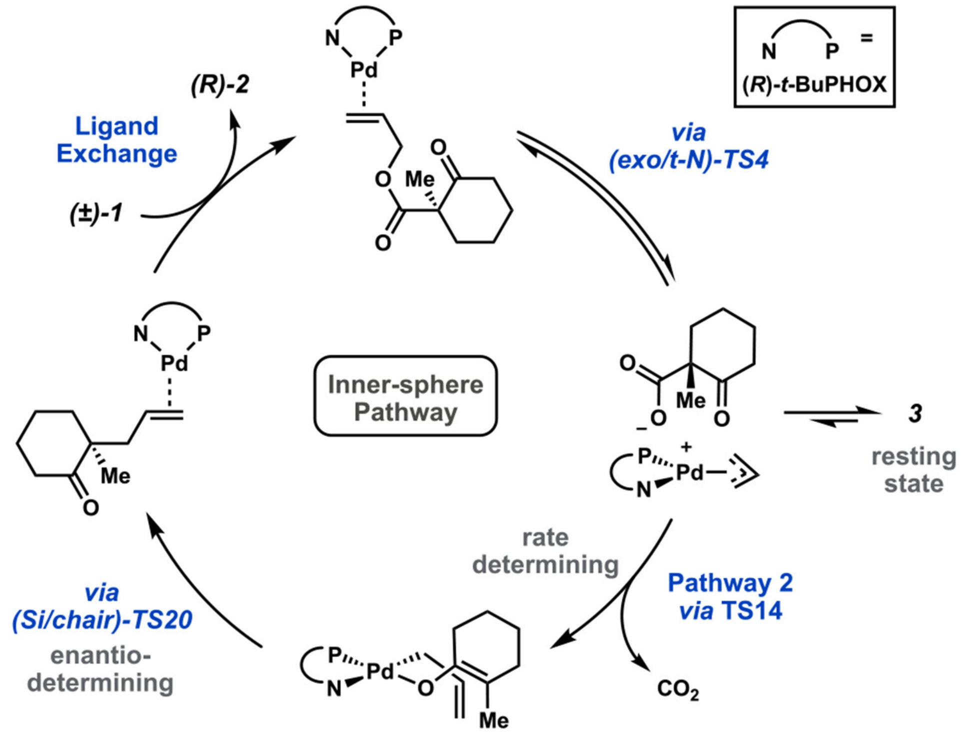

Figure 12.

Complete catalytic cycle for the allylic alkylation reaction.

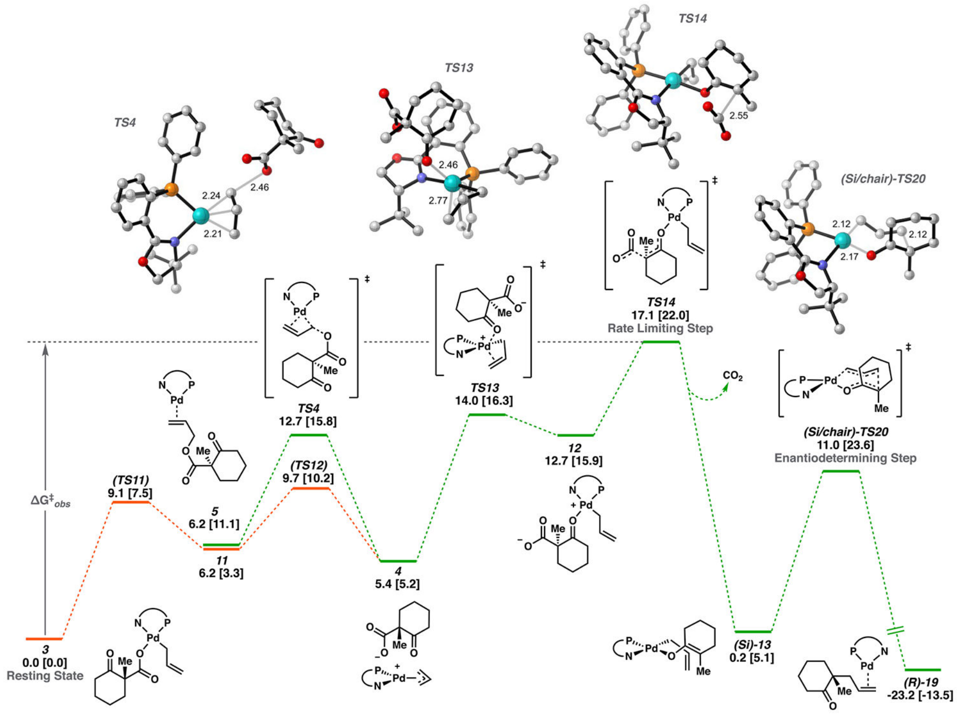

Figure 13.

Free energy profile of minimum energy pathway through full catalytic cycle (green) as well as pathway for equilibration to off cycle resting state **3** (orange). Note that decarboxylation is considered irreversible as CO_2 is lost to reaction headspace/atmosphere.

Author Manuscript Author Manuscript Author Manuscript Author Manuscript

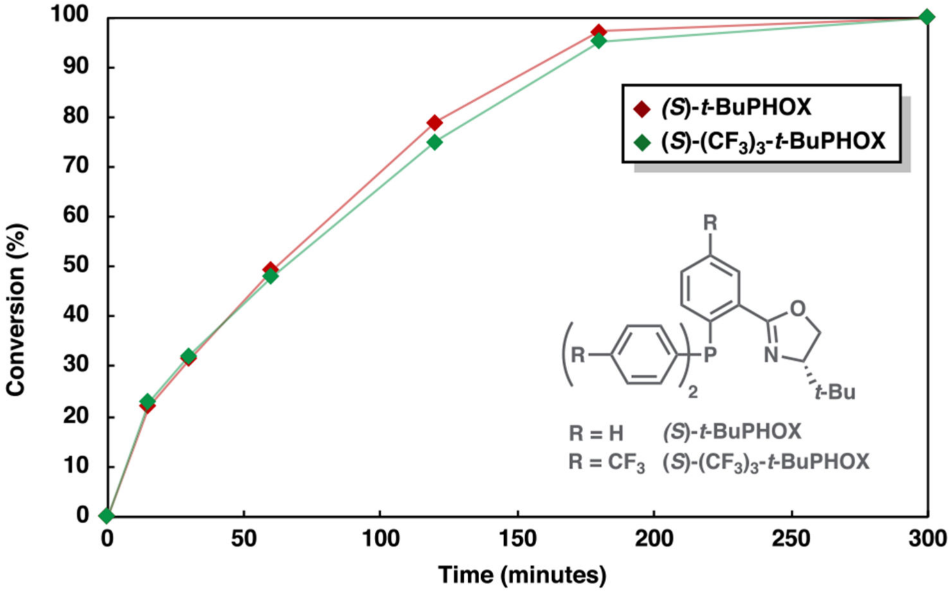

Figure 14.

Time course of conversion of **1** to (***S***)**-2** under standard conditions with the (*S*)-*t*-BuPHOX and (*S*)-(CF_3)$_3$-*t*-BuPHOX ligands. Conversion as determined by GC-FID with respect to tetradecane internal standard.

Author Manuscript
Author Manuscript
Author Manuscript
Author Manuscript

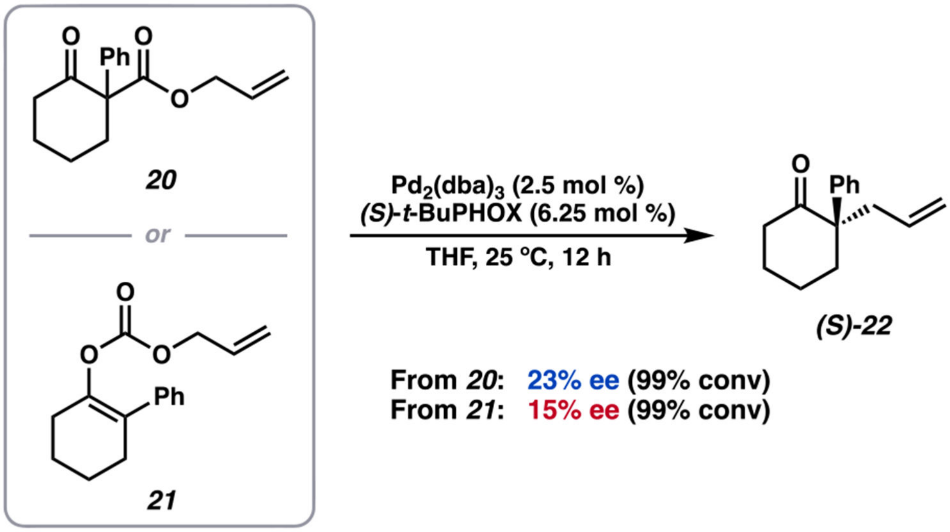

Figure 15.

Standard conditions for the decarboxylative asymmetric allylic alkylation as investigated herein applied to substrates that afford a stabilized α-phenyl palladium enolate.

Author Manuscript Author Manuscript Author Manuscript Author Manuscript

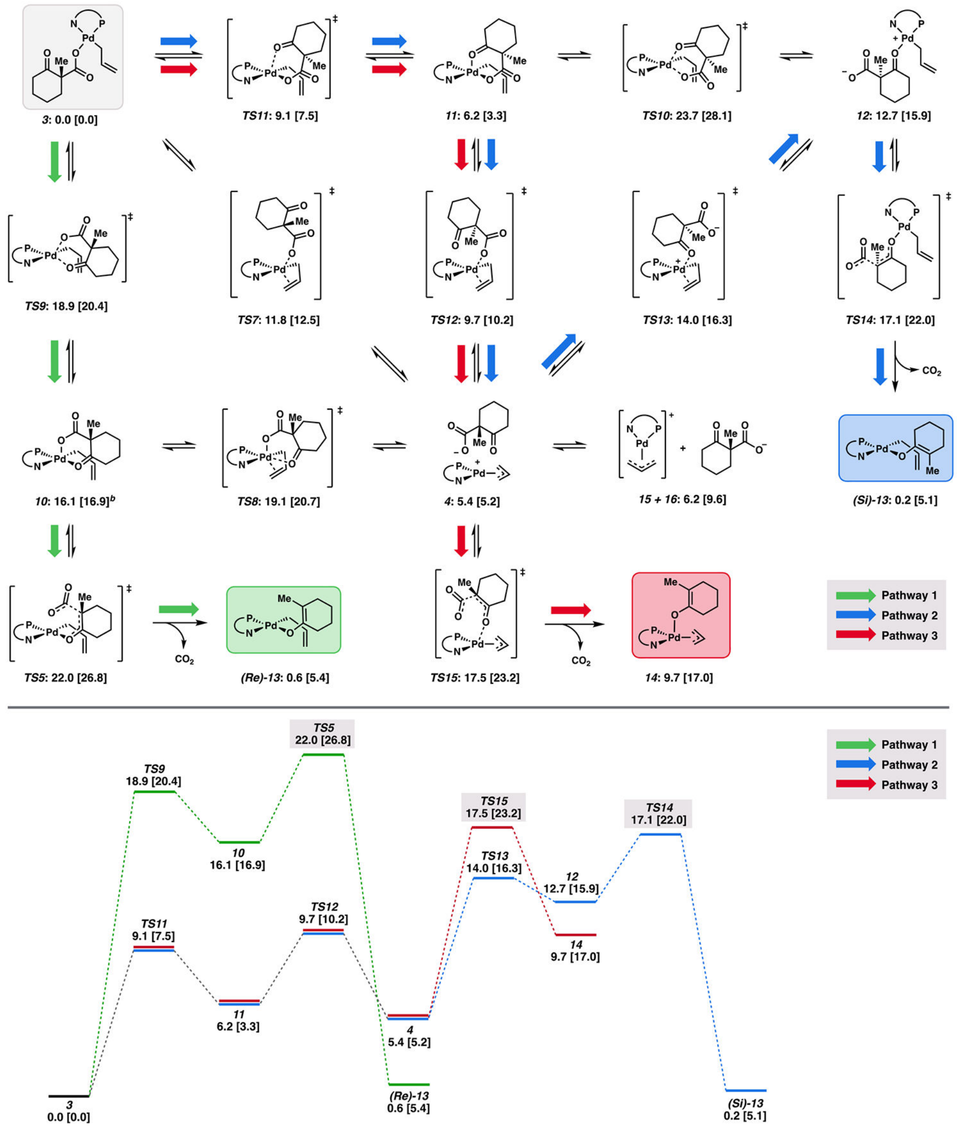

Scheme 1.

Free Energy Network of Intermediates from Oxidative Addition Products and Catalyst Resting State through Decarboxylation to Palladium Enolates[a]

[a]Free energy network from derived the (*R*) enantiomer of starting material **1**. Relative free energies (in kcal/mol) obtained with M06/def2-TZVP–CPCM(THF), with energies at the DLPNO-CCSD(T)/cc-pVTZ–CPCM(THF) level of theory in brackets. Lowest energy conformers depicted. [b]Free energy of lowest energy conformer obtained with DLPNO-CCSD(T) corresponds to chair flip of the lowest energy conformer obtained with M06.

Author Manuscript Author Manuscript Author Manuscript Author Manuscript

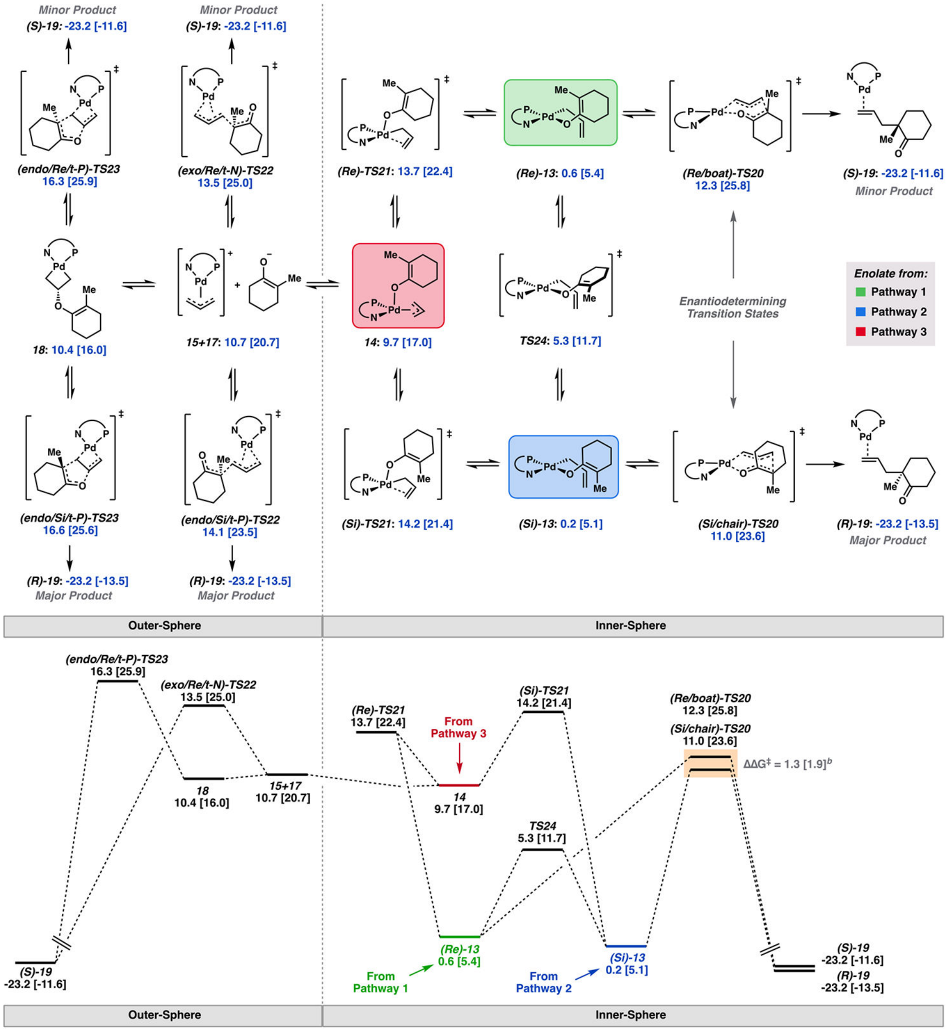

Scheme 2.

Free Energy Network Connecting Various C—C Bond Forming Pathways[a]

[a]Free energy network of postdecarboxylation intermediates and key C—C bond forming transition states. Free energies relative to **3** (in kcal/mol) obtained with M06/def2-TZVP–CPCM(THF), with energies at the DLPNO-CCSD(T)/cc-pVTZ–CPCM(THF) level of theory in brackets. Lowest energy conformers depicted. [b]$\Delta\Delta G^{\ddagger}$ refined to 1.9 kcal/mol with TightPNO settings.

Author Manuscript Author Manuscript Author Manuscript Author Manuscript

Table 1.

Comparison of Relative Free Energy Barrier Heights along Reductive Elimination Pathways[a]

Intermediate	PhMe	Et_2O	THF	DMF
(*Re*)-13	0.6	0.5	0.5	0.4
(*Si*)-13	0.0	0.0	0.0	0.0
14	8.8	9.3	9.5	9.8
15 + 17	33.2	17.5	9.2	−0.5
(*Re*)-TS21	13.5	13.5	13.5	13.6
(*Si*)-TS21	14.1	14.1	14.1	14.1
(*Si*/chair)-TS20	9.5	10.3	10.8	11.5
(*Re*/boat)-TS20	10.9	11.7	12.1	12.7
(endo/*Si*/*t*-P)-TS22	14.9[b]	13.9[b]	13.3	12.6
(exo/*Re*/*t*-N)-TS22	16.0[b]	14.7[b]	13.9	12.9
(endo/*Si*/*t*-P)-TS23	19.8	17.8	16.6	15.1
(endo/*Re*/*t*-P)-TS23	19.1	17.2	16.1	14.8

[a] Relative free energies given in kcal/mol at the M06/def2-TZVP–CPCM(*solvent*) level of theory on geometries obtained in the gas phase.

[b] Barrier less than free energy of separated ions **(exo)-15** and **17**.

Author Manuscript Author Manuscript Author Manuscript Author Manuscript

Table 2.

Effects of Solvation and Ligand Electronics on Enantioselectivity

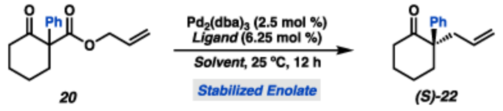

Entry	Ligand	Solvent [ε]	ee (%)[a]	Yield *22* (%)[b]	ΔG_{eq}[c]
1	(*S*)-*t*-BuPHOX	THF [7.4]	23	99	1.8
2	(*S*)-*t*-BuPHOX	PhMe [2.4]	28	96	24.0
3	(*S*)-$(CF_3)_3$-*t*-BuPHOX	PhMe [2.4]	32	90	31.0
4	(*S*)-$(CF_3)_3$-*t*-BuPHOX	2:1 MeCy/PhMe [2.1]	36	69[d]	35.2

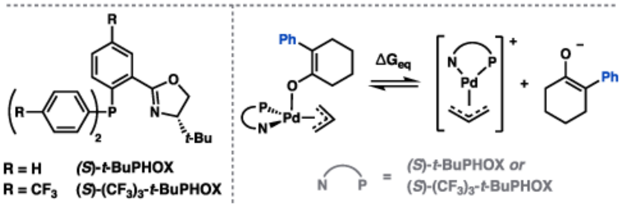

[a] Obtained by chiral SFC.

[b] Determined by ^{1}H NMR with respect to internal standard.

[c] Change in free energy (in kcal/mol, 1 M standard state) from square pyramidal enolate to free ions.

[d] 34% **20** remaining after 12 h (^{1}H NMR with respect to internal standard).